(front cover sample)

Dynamic nuclear polarization of ^{29}Si nuclei using lithium related centers in isotopically controlled silicon

February 2011

Rahman Mohammad Rizwanur

(spine sample)

Dynamic nuclear polarization of ^{29}Si nuclei using lithium related centers in isotopically controlled silicon

Februarv 2011 Rahman Mohammad Rizwanur

A Thesis for the Degree of Ph.D. in Technology

Dynamic nuclear polarization of ^{29}Si nuclei using lithium related centers in isotopically controlled silicon

February 2011

Graduate School of Science and Technology
Keio University

Rahman Mohammad Rizwanur

Abstract

Quantum computers (QC), if realized, can overwhelm the performance of conventional computers in a number of calculational tasks. A hydrogenic donor in silicon is one of the most promising candidates as a fundamental building block of QC referred to as a quantum bit (qubit) towards realization of future solid-state QC. Application of donors as qubits requires in-depth understanding of their structural, electronic, and magnetic properties. Moreover, control of their interactions with nuclear spins in silicon matrix is needed.

The present thesis reports investigations of magnetic properties of lithium (Li) hydrogenic donor related centers in silicon by electron paramagnetic resonance (EPR) spectroscopy and dynamic nuclear polarization (DNP) of host ^{29}Si using lithium related centers in isotopically controlled silicon. Lithium is the only non-substitutional hydrogenic donor in silicon that forms a complex pair with an oxygen atom very easily. Thanks to its low ionization energy and inverted ground state energy levels, long electronic spin decoherence time (T_2) and short electron relaxation time (T_1) that are favorable for construction of QC are expected.

The present thesis is composed of six chapters. Chapter 1 is an introduction and 2 provides a literature survey on lithium related centers in silicon. Chapter 3 provides basic principles of magnetic resonance. Chapter 4 discusses EPR of lithium related center in silicon. Significant narrowing of the isolated Li EPR and additional hyperfine structures of lithium-oxygen (Li-O) centers were observed in isotopically enriched ^{28}Si single crystals. Unexpected splitting was found reflecting the principal axis of the formally assigned trigonal *g*-tensor being 3^o tilted from <111> crystal axis, i.e., the g-tensor of the Li-O center actually has a monoclinic symmetry. Furthermore splitting of ^{7}Li hyperfine lines into four components was observed at temperatures 3.5 K. These findings provided accurate knowledge of EPR frequencies of Li related centers that are needed for high fidelity operation of Li quantum bits in silicon. Chapter 5 reports dynamic nuclear polarization (DNP) of ^{29}Si nuclear spins induced by saturation of EPR transitions of lithium-related centers. Both isolated Li and Li-O complex centers showed strong EPR absorption lines in the temperature range 3.4-10 K and led to very efficient orientation of

^{29}Si nuclear spins. The temperature dependence and time constant of ^{29}Si DNP are investigated in detail. The ^{29}Si DNP of 0.72 % was achieved at 3.4 K by excitation of the Li-O forbidden EPR transition under illumination, corresponding to a ~352 fold increase with respect to the thermal equilibrium polarization. Possible strategies are discussed to obtain >5% ^{29}Si DNP that is needed for realization of quantum computing. Chapter 6 provides conclusions and outlook.

Acknowledgement

This thesis arose in part out of years of research that has been done since I came to Itoh's group. By that time, I have worked with a great number of people whose contribution in assorted ways to the research and the making of the thesis deserved special mention. It is a pleasure to convey my gratitude to them all in my humble acknowledgment.

In the first place I would like to record my gratitude to Prof. Kohei M. Itoh for his supervision, advice, and guidance from the early stage of this research as well as giving me extraordinary experiences throughout the work. Above all and the most needed, he provided me unflinching encouragement and support in various ways. His truly scientist intuition has made him as a constant oasis of ideas and passions in science, which exceptionally inspire and enrich my growth as a student, a researcher and a scientist.

I gratefully acknowledge Prof. L. S. Vlasenko and Dr. M. P. Vlasenko for their advice, supervision, and crucial contribution, which made my backbone of this research and so to this thesis. His involvement during experiment with his originality has triggered and nourished my intellectual maturity that I will benefit from, for a long time to come.

I am thankful to Prof. M. Uematsu and Dr. T. Sekiguchi for their support useful suggestion degrading lithium diffusion. When I started my work on lithium in silicon I am much indebted to Prof. E. E. Haller in September 2007 during his stay at Keio University.

Thanks, therefore, to: Itahashi Tatsumasa for knowing all that's worth knowing about electron spin resonance and dynamic nuclear polarization experiment, and teaching me about some of it. Although few of the group members were directly involved in my project, their research activities, spirits, opinions, and other right things affected me in several ways, and all the other past and present group members are worthy of acknowledgements. From the past members,

Yasuo Shimizu, Satoru Miyamoto, Hiroshi Hayashi, Hiroki Morishita, Itahashi Tatsumasa, Youhei Shiren, Shinichi Tojo, Hiroyuki Tezuka, Masashi Hirose, Nao Harada, Mohammad Waseen Akhtar Toyofumi Ishikawa, Yoko Kawamura, Miki Nganawa, Kei Yoshizawa, Shinchan Hong Agung, Luis Jou Garcia, Rii Hirano, Katsuhiko Naito, Go tsuchiya, Yuri Sakuma, Kei Koga, Tomoya Arai, Sanae Iida, and Masakazu Kashiwabara. I also thank those I gratefully thank Waseem and Hiroki for their constructive comments on this thesis. I would like to thank my entire friend from elementary school day till my Keio University who help me in very stage and for their support.

Where would I be without my family? My parents deserve special mention for their inseparable support and prayers. My Mother, in the first place is the person who raised me and put the moral values and my father I would say about him that he is "*my role model*" not because he is my father but many quality make him very special which keep him apart from league. He is a true inspiration for me. I would like to thank my brother and sister for giving me moral, unconditional support and affection.

Contents

Chapter 1

Introduction

1.1 Background and motivation

Computational performance of classical computers is limited by the number of transistors that can be positioned on an integrated circuit. According to Moore's law, there will be a time when the size of each transistor reduces to an atomic scale, which will not permit the classical physics to predict the behavior of the system. At the present technology the classical computer is unable to factor integers of more than 1000 bit in reasonable time frame even with the best algorithm. Hence the new concept of computer based on the principle of quantum mechanical effect is needed to be developed. In contrast to classical computing, quantum computing is based on the *quantum mechanical principles* such as *superpositions* and *entanglements.* The essence of a quantum computer is the use of quantum bits (qubits) where the quantum states can be represented by the superposition states of "spin up" (1) and "spin down" (0). Shor's algorithm [1, 2] of quantum computing is capable of prime factorization much faster than the classical computer. Other important applications include database search [3] and quantum mechanical simulation [4].

For the realization of quantum computers, there are five requirements outlined by Deutsch and DiVincenzo [5, 6]:

1) Employment of a well characterized qubit in a physical structure.
2) Initialization of the qubits into fiducial states such as $|000..\rangle$ or $|111\ldots\rangle$.
3) Long enough decoherence time of qubits to complete an algorithm.

4) Ability to perform an universal set of quantum gates.
5) Ability to perform a qubit–specific measurement with high fidelity.

A variety of quantum bits (qubits) have been proposed as potential candidates. They include electron spins in solids [7 – 11], trapped ions in vacuum [12], photons in air [13], charges or fluxes in superconducting circuits [14], ions in cavities [15], Bose–Einstein condensates [16], quantum dots [17], superconducting loops [18], excitons in solids [11, 19], nuclear spins in solids [6, 7, 20 – 23], etc. There is a group of researchers who believe that silicon based quantum computers [7, 24] are promising candidates for large scale quantum computers because of the availability of state–of–the–art silicon processing technologies that are essential for making the quantum computer integrated. A representing example of the silicon quantum computer was proposed by Kane [7]. Kane's quantum computer utilizes an array of phosphorus donors as qubits which are embedded at a depth of 20 nm in a ^{28}Si isotopically enriched silicon substrate. The quantum state of each qubit can be controlled by irradiation of rf–fields which induces magnetic resonance. Application of electrostatic bias at the surface just above each qubit (A–Gate) tunes the hyperfine interaction strength to induce or not to induce the resonance that corresponds to a rotational or phase gate. Surface electrodes placed between the adjacent qubits (J–Gates) control electron–electron exchange interaction. By this control two–qubit operations between adjacent qubits can be performed selectively. Figure 1.1 (a) shows the Kane's quantum computer architecture. Kane's scheme faces three major challenges: 1) Placement of an array of phosphorus donors in silicon. 2) Formation of electrodes and calibration of interactions to achieve high fidelity gate operations. 3) Realization of a single nuclear spin measurement.

Following Kane's proposal, a number of silicon–based quantum computing schemes has been proposed. Among them, the idea of utilizing lithium donors is most relevant to this thesis. An interstitial lithium takes T_d–site symmetry in silicon and has fivefold degenerate ground state $1s(E + T_2)$ with a fully symmetric state $1s(A_1)$ separated by 1.76 meV. The site symmetry reduces from T_d to D_{2d} by application of uniaxial stress. The fivefold degenerate state then becomes non–degenerate with the ground state an odd parity and the first excited state an even parity. A weak coupling between the opposite parity states by phonons induces relaxation from the first excited state to ground state in the time frame of the order of 1000 sec. This long relaxation gives an opportunity for the quantum information processing by application of controlled ac or dc

external stress. The quantum information processing based on lithium charge qubits was proposed by Smelyanskiy *et al.* [24]. In this scheme lithium donor atoms are embedded in a silicon single crystal with a separation distance of d = 100 nm. Chernyak *et al.* have shown that it is possible to fabricate the array of lithium atoms via electromigration technique [25]. This scheme utilizes three electrodes A_1, B_1, and C_1 for the application of ac and dc electric fields in different stages. The piezoelectric film (light green) is deposited on *n*–type heavily doped nanowire (C_1) to control the external stress on the array of Li atoms. The schematic representation of a lithium based quantum computer is shown in Fig. 1.1 (b).

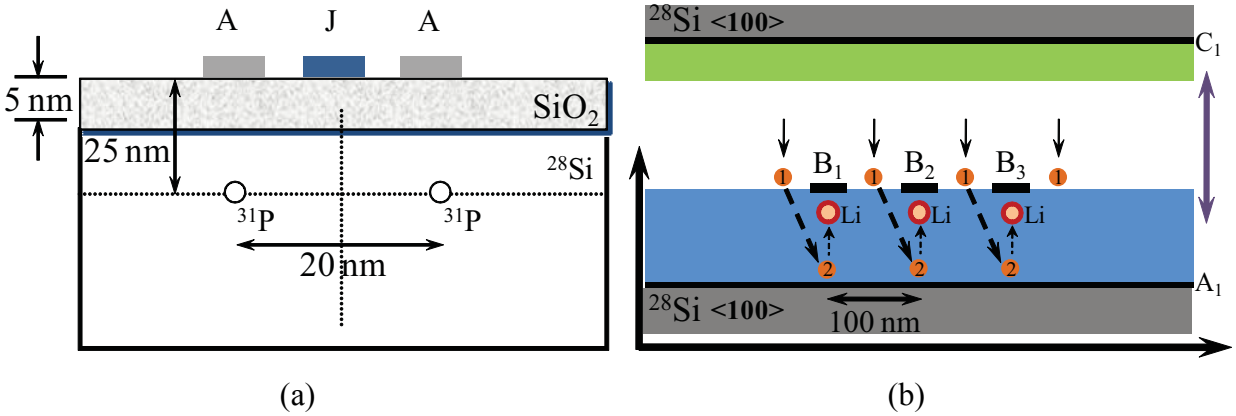

Figure 1.1: (a) Schematic of Kane's architecture. This scheme utilizes an array of phosphorus donors embedded at a depth of 25 nm from the surface of a ^{28}Si single crystal. Neighboring qubits are separated by 20 nm. The *A*–gates are placed above qubits, while *J*–gates are placed between them. (b) Schematic representation of a Si:Li based quantum computing scheme. An array of lithium donors is placed between the electrodes A_1 and B_1 in an isotopically enriched silicon. The piezoelectric film (light green) is sandwich between electrode B_1 and C_1 to apply tailored pulses of stress.

In this scheme the quantum logical operation does not rely on the single qubit read out operation but work on a long–range elastic–dipole interaction between qubits. The long range elastic–dipole interaction depends on the inter–qubit distance R as R^{-3} or R^{-5}. In the charge based quantum computer, decoherence rate is governed by the charge fluctuations in the surrounding environment. An error of the two–qubit gates due to decoherence is also small. In reality, relaxation of the charge traps induced by a shot noise leads to decoherence times that is

significantly shorter than the scheme based on spin of qubits. Therefore it is important to explore and understand the spin states of lithium in silicon. Lithium donors in isotopically enriched ^{28}Si are of special interest because depletion of ^{29}Si nuclear spins is expected to enlong decoherence time of lithium electron spins.

1.2 Purpose of the present work

The main purpose of this work is to study the symmetry and microstructure of lithium and lithium–oxygen centers in isotopically enriched ^{28}Si samples. It is important to enhance our understanding of the lithium related centers in silicon because an isolated lithium interstitial shallow donor was also proposed to be an attractive candidate of a qubit in silicon [24]. However, it is not experimentally straightforward to introduce lithium atoms exclusively into isolated interstitial sites. Instead Li–O complexes that involve residual oxygen impurities are easily formed. The Li–O centers in silicon are also shallow donors with the ionization energy 39.41 meV [26, 27]. Therefore, it is importance to understand the symmetry of magnetically active centers like Li–O centers especially in silicon that are depleted of ^{29}Si nuclear spins, e.g., in isotopically enriched ^{28}Si single crystals.

In parallel, there are cases where depletion of ^{29}Si nuclear spins is difficult or employment of ^{29}Si nuclear spins as qubits is desired. In such a case, active control of ^{29}Si nuclear spin states by manipulation of lithium electron spins is needed. Achieving the polarization 5 % and larger is required to initialize ^{29}Si nuclear spin qubits at the beginning of quantum computing. Dynamic nuclear polarization (DNP) is one of promising methods to achieve a high degree of the ^{29}Si nuclear polarization by transferring the equilibrium Boltzmann electron polarization to the ^{29}Si nuclei. Obtaining high nuclear polarization by DNP requires low temperatures and strong magnetic fields. Previously carried out DNP experiments with phosphorus doped silicon achieved ^{29}Si polarization of 0.28 % in a naturally abundant silicon sample at 12 K but this was limited by the long relaxation time of electrons bound to phosphorus donors ($\approx 3\times10^3$ s at 1.2 K) [26, 27, 28]. Much shorter spin–lattice relaxation time expected for electrons bound to Li related centers in silicon at $T < 10$ K makes Li an attracting candidate as a ^{29}Si DNP mediator.

1.3 Organization

This thesis is organized as follows. Chapter 1 introduces the motivation and purpose of the dissertation. Chapter 2 is the literature review of lithium related centers in silicon. Here an unsolved problem related to symmetry of lithium related centers in silicon is identified. Chapter 3 is an overview of the magnetic resonance principle. Chapter 4 shows the electron paramagnetic resonance (EPR) study of lithium related centers in isotopically controlled silicon. EPR of lithium related centers in naturally abundant silicon is shown in section 4.2.2. EPR of lithium related centers in a isotopically enriched ^{28}Si sample is discussed in section 4.2.4. A new results concerning symmetry of Li–O complex is discussed in section 4.3. Chapter 5 shows the dynamic nuclear polarization (DNP) of ^{29}Si nuclear spins by saturation of EPR forbidden transitions of lithium related centers. Dependences of the ^{29}Si nuclei polarization on parameters such as temperature, saturation time, and magnetic field are discussed in section 5.2. Possible strategies to enhance the DNP further using Li related centers are discussed in section 5.3. Chapter 6 provides conclusion.

Chapter 2

Lithium in silicon

2.1 Introduction

A lithium related center forms a donor in silicon. They come in two forms; interstitial neutral lithium (Li^0) and lithium–oxygen (Li–O) centers due to lithium's strong affinity with oxygen. Ionization energies of Li^0 and Li–O centers are 33 meV and 39 meV, respectively [31 – 33].

In 1939 Jackson and Kuhn investigated the hyperfine splitting and Zeeman splittings of the resonance line of the two stable isotopes of lithium. By means of the atomic beam absorption they observed 3 and 4 hyperfine lines for ^{6}Li ($\boldsymbol{I}$ = 1) and ^{7}Li ($\boldsymbol{I}$ = 3/2) isotopes, respectively, which was consistent with the relation $2\boldsymbol{I}$ + 1 [34]. They calculated the nuclear magnetic moments to be 0.820 and 3.25 for ^{6}Li and ^{7}Li, respectively [34, 35]. The purposes of studying lithium in silicon in 1960s and 1970s were motivated by the developments of semiconductor detectors for nuclear physics [36 – 40], solar cells [33, 41], and marker to detect low concentrations of oxygen contents in silicon [36]. Other investigations [42 – 45] were devoted to the local placements of lithium in silicon, e.g. at the positions of to grown–in extended defects and clusters of the impurities. Further interest arose from the peculiarity of the lithium donor having a degenerate orbital ground state, which was systematically investigated by optical measurements [27] and electron spin resonance [46, 47].

The isolated neutral lithium (Li^0) in silicon and germanium is mobile even at room temperature; it jumps from one interstitial equilibrium site to another site with very little lattice distortion due to its small ionic radius (0.60 Å) with respect to the host crystal element [48]. Therefore lithium

is a highly diffusive donor in silicon, e.g., diffusion coefficient of the order of 10^{-7} cm^2 s^{-1} even at 500ºC [32]. Diffusion of lithium in silicon was extensively studied by measuring the position of a *p–n* junction as lithium impurities were diffused into *p*–type samples [49 – 51].

Pell investigated the interaction between the isolated interstitial lithium and electrically inactive interstitial oxygen in silicon [52] by the kinetic analysis of the precipitation process. The reaction between the lithium and oxygen is described by;

$$LiO^+ \leftrightharpoons Li^+ + O \qquad (2.1\ a)$$

Equation (2.1 a) can be written in terms of the concentrations and a dissociation constant, *C*:

$$[LiO^+]C = [Li^+]\,[O] \qquad (2.1\ b)$$

where the dissociation constant being 4×10^{23} $\exp(-0.52q/kT)$ $atom.cm^{-3}$. Ham's theory of diffusion limited precipitation explained the behavior of the carrier concentration by lithium precipitation in silicon when the oxygen concentration was more than 10^{16} cm^{-3} [53]. Pell concluded that the precipitation of Li was easily overwhelmed by the interaction of lithium with oxygen. The lithium–oxygen center is a donor and is not mobile in silicon at room temperature. Pell measured the electrical conductivity vs. time subsequent to rapid quenching from high temperature at which lithium was diffused into the sample. Important findings are:

I) The precipitation of Li in CZ silicon occurs when the Li concentration exceeds10^{17} cm^{-3}. Li form the Li–O centers when the concentration of Li is less than one fifth of the oxygen content. However lithium precipitates when its concentration reaches more than one fifth of the oxygen concentration.

II) The lithium diffusion rate changes when Li form Li–O.

III) Higher order of lithium oxygen complexes (Li_mO^{n+}) exist at supersaturation of lithium.

Pell investigated the possibility of producing a large volume of intrinsic silicon by diffusing lithium atoms into *p*–type silicon and drifting them in the ionic forms throughout the sample [54]. A successful production of a large volume of silicon in this manner led to very sensitive

nuclear detectors. The high diffusion coefficient of lithium in silicon was the key for the construction of Si:Li detectors. Lithium–oxygen interaction can be used to measure the oxygen content in silicon by probing the intensities of 9 μm infrared absorption [55, 56]. The precipitation rate of the Li–O center [53] can be used to measure the oxygen content down to 10^{15} cm^{-3}.

2.2 Symmetry of lithium related centers

Wert and Zener proposed the theory for diffusion of interstitial atoms in metals which can be extended to semiconductors [57]. It estimated the entropy of diffusion when the strain increases the entropy of the lattice [58]. Later, Swalin *et al*. proposed the theory for diffusion of substitutional donors in silicon` [59]. Weiser proposed a model to determine the symmetry of an interstitial natural donor [60]. Here it was assumed that a lattice distortion contributes by 10% to the activation energy of diffusion in a diamond lattice. Then they calculated the activation energy based on the interaction of the impurity with the host atoms.

Figure 2.1 shows two preferential interstitial sites; (a) a tetrahedral site which is characterized by four nearest host atoms with the distance of $0.433a_0$ from the center, and six next–neighbors with the distance of $0.500a_0$, (b) a hexagonal site with the distance of $0.415a_0$ from the six host atoms, and $0.649a_0$ from the eight next–nearest neighbors, where a_0 is the unit cell edge length [61]. The impurity atom in the crystal prefers an as high symmetry point as possible because at the symmetric site the impurity atom is equally far away from the host atoms so that the repulsive force will be minimal. This trend becomes more pronounce for the case of a small particle such as lithium. The repulsive energies U_{rep} in eV of the lithium ion at the center of the tetrahedral and of hexagonal cavities are derived by Born–Mayer equation [62];

$$U_{rep} = 4A\ exp(r_L + r_I - r_T)/\rho + 6A\ exp(r_L + r_I - 1.15r_T)/\rho, \quad \text{(tetrahedral site)} \quad (2.2\ a)$$

$$U_{rep} = 6A\ exp(r_L + r_I - r_H)/\rho + 8A\ exp(r_L + r_I - 1.56r_H)/\rho, \quad \text{(hexagonal site)}, \quad (2.2\ b)$$

where, A = 0.63, r_L = 0.117 nm is the effective radius of a silicon atom [63], r_I = 0.06 nm is the ionic radius of the lithium atom [48], and r_T and r_H are distances from the center of each symmetry to the nearest host atom for the tetrahedral and hexagonal cases, respectively.

From equation (2.2) it is estimated that the contribution to the repulsive force of the next–nearest neighbors in the tetrahedral case is 50 %, while in the case of hexagonal is only 2 %. The repulsive force at the hexagonal site due to the host atom is higher by 0.038 exp(r_I / ρ) than the tetrahedral sits. Therefore the tetrahedral site is more preferable than the hexagonal site. If the lithium ion site away from the symmetric site, the polarization energy must be estimated. The polarization energy is expressed in terms of spherical harmonics (equation (2.3)) [64]. It is shown that the hexagonal site has the total polarization energy lower than the tetrahedral site by 0.05 eV based on an equation;

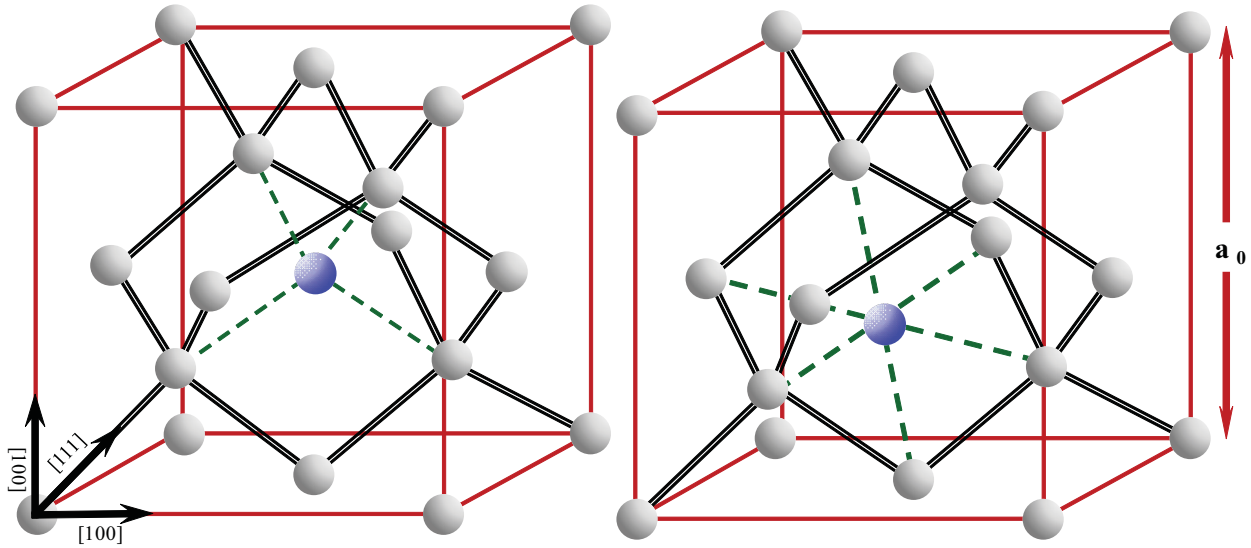

(a) (b)

Figure 2.1: Atomic structure of a diamond type crystal with lattice constant a_0. (a) Tetrahedral site symmetry with the nearest neighbors at 0.433a_0, and the next–nearest neighbors at 0.500a_0. (b) Hexagonal site symmetry with the nearest neighbors at 0.415a_0 and the next–nearest neighbors at 0.649a_0.

$$-U_{pol} = \frac{q^2}{2R_c}\left(1 - \frac{1}{K}\right) \times \left[1 + \frac{2}{3}\frac{\partial^2}{R_c^2} + higher\ powers\ in\ \left(\partial/R_e\right)\right], \qquad (2.3)$$

where, q is the charge of the particle, ∂ is the displacement of the charge from the center of the cavity of radius R_e, and K is the dielectric constant of the material.

Weiser found in his calculation that the electrostatic polarization energy dominates over the energy of overlap repulsion, so that the hexagonal site with its six silicon neighbors is favored over the tetrahedral site. In contrast to Weiser, theoretical calculation by Bellomonte *et al*. on the basis of localized vibration modes shows that the overlap repulsion dominates and the hexagonal site has higher overlap repulsion than the tetrahedral site because of the higher density of the hexagonal site [65, 66]. Therefore a detail study is needed to find out the site symmetry of Li in diamond type crystal.

Aggarwal *et al*. were the first to study the excitation spectra of lithium related centers in silicon [27]. An excitation spectrum of lithium was observed in oxygen free silicon (FZ silicon) to conclude that the ground state was different from the substitutional site. The $1s(A_1)$ state was found 1.8 meV above the $1s(E + T_1)$ state. The excitation spectrum of Li–O centers in crucible grown silicon (oxygen concentration of the order of 10^{17} cm^{-3}) was obtained and found that the ground state is the same as the substitutional donors. The $1s(E + T_1)$ state situates 7.7 ± 0.1 meV above the $1s(A_1)$ state. The site symmetry of the lithium–oxygen center and isolated lithium were tetrahedral (T_d).

Figure 2.2 (a) shows the excitation lines of isolated lithium recorded with externally applied stress $\vec{\boldsymbol{F}}$ in [100] direction and polarization $\vec{\boldsymbol{E}}$ of the light also in [100] direction [27]. Figure 2.2 (b) shows the same spectroscopy with $\vec{\boldsymbol{E}} \perp \vec{\boldsymbol{F}}$ [27]. Figure 2.2 (c) shows a corresponding energy diagram [67, 68] and Table 2.1 shows corresponding energy spacings. If the chemical splitting for isolated lithium is zero, it is clear that the excitation lines will not split under the application of uniaxial stress. However as shown in Fig. 2.2 (c), the ground state splits into three components. With the above choice of ground–state structure, for the case of F ‖ [100] and F ‖ [110], the site symmetry of the interstitial lithium changes from T_d to that of D_{2d} and C_{2v}, respectively [69].

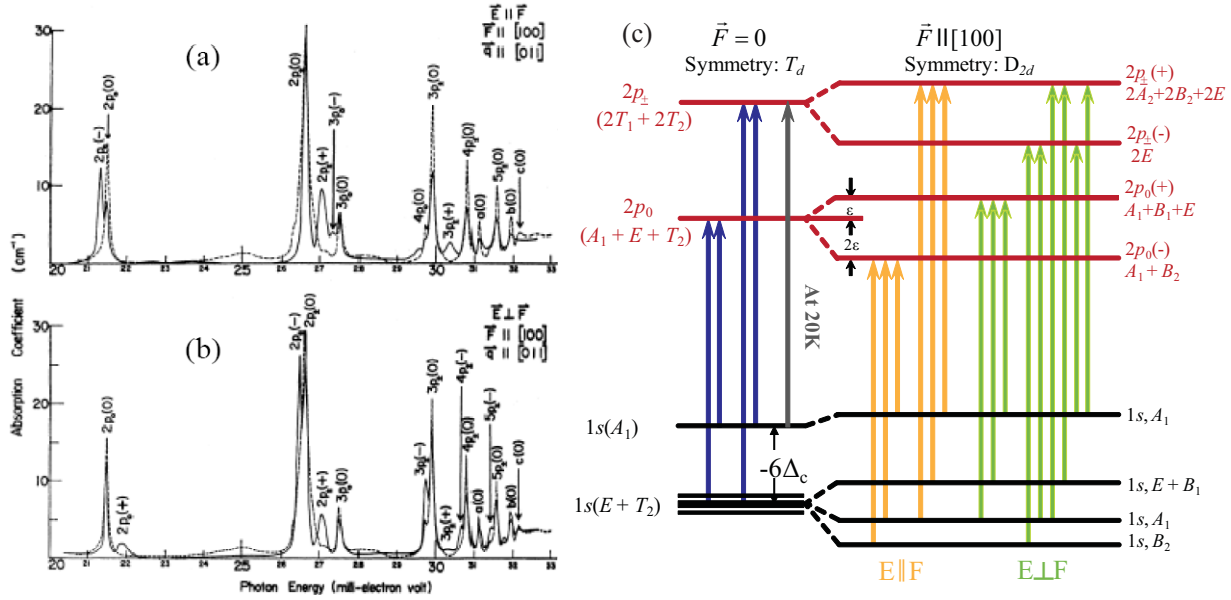

Figure 2.2: The effect of a [100] compression on the excitation spectrum of Li^0 for the direction of light propagation (q) is along [011] for (a) E ∥ F and (b) E ⊥ F. The dashed curves in (a) and (b) are for F = 0 (c) Splitting of the donor levels in silicon (not to scale) under a [100] compression for a finite $6\Delta_c$ and with an "inverted" Group–V–like ground state. The vertical arrows indicate the allowed transitions. The capital letters labeling the levels denote the irreducible representations of T_d and D_{2d} to which the states belong [27].

Similarly, the Li–O center excitation spectra under uniaxial stress and excitation energy level diagram are shown in Fig. 2.3 (a) and (b). These excitation spectra are very similar to that of Group–V impurities [70 – 72]. The zero stress linewidths of Li–O and phosphorus are 0.025 and 0.026 meV, respectively [72]. The energy level diagram is shown in Fig. 2.3 (c).

In the framework of the effective–mass approximation and deformation potential theory, comparison of the excitation spectra under stress between substitutional donors and Li–O centers confirms that the site symmetry is tetrahedral (T_d) in the absence of stress and that the lowest ground state of the Li–O centers is $1s(A_1)$ [31, 67, 69, 73]. The chemical splitting of Li–O is 7.7 meV. In conclusion, the excitation spectra of lithium related centers show that its site symmetry is tetrahedral (T_d) instead of hexagonal. The ground–state of Li^0 and Li–O center are $1s(E + T_2)$ and $1s(A_1)$, respectively.

Table 2.1: The energy of excited lines of isolated lithium (Li^0) and lithium–oxygen centers (Li–O) in meV. x_1, x_2, x_3, x_4 a, b, and c are unidentified peaks.

Li^0			Li–O		
Label	Assignment	Energy	Label	Assignment	Energy
$2p_0$	$1s(E + T_1) \rightarrow 2p_0$	21.50	$1s(E + T_1) \rightarrow 2p_\pm$	$1s(E + T_2) \rightarrow 2p_\pm$	25.60
$1s(A_1) \rightarrow 2p_\pm$	$1s(A_1) \rightarrow 2p_\pm$	24.50	x_1	?	26.63
$2p_\pm$	$1s(E + T_1) \rightarrow 2p_\pm$	26.63	$2p_0$	$1s(A_1) \rightarrow 2p_0$	28.10
$3p_0$	$1s(E + T_1) \rightarrow 3p_0$	27.51	x_2	?	29.08
$4p_0$	$1s(E + T_1) \rightarrow 4p_0$	29.72	x_3	?	31.86
$3p_\pm$	$1s(E + T_1) \rightarrow 3p_\pm$	29.91	x_4	?	32.45
$4p_\pm$, $5p_0$	$1s(E + T_1) \rightarrow 4p_\pm$, $5p_0$	30.82	$2p_\pm$	$1s(A_1) \rightarrow 2p_\pm$	33.33
A	?	32.12	$3p_0$	$1s(A_1) \rightarrow 3p_0$	34.14
$5p_\pm$	$1s(E + T_1) \rightarrow 4p_\pm$	31.56	$4p_0$	$1s(A_1) \rightarrow 4p_0$	36.35
B	?	31.94	$3p_\pm$	$1s(A_1) \rightarrow 3p_\pm$	36.51
C	?	32.16	$4p_\pm$, $5p_0$	$1s(A_1) \rightarrow 4p_\pm$, $5p_0$	37.47
Ionization energy		32.81	Ionization energy		39.41

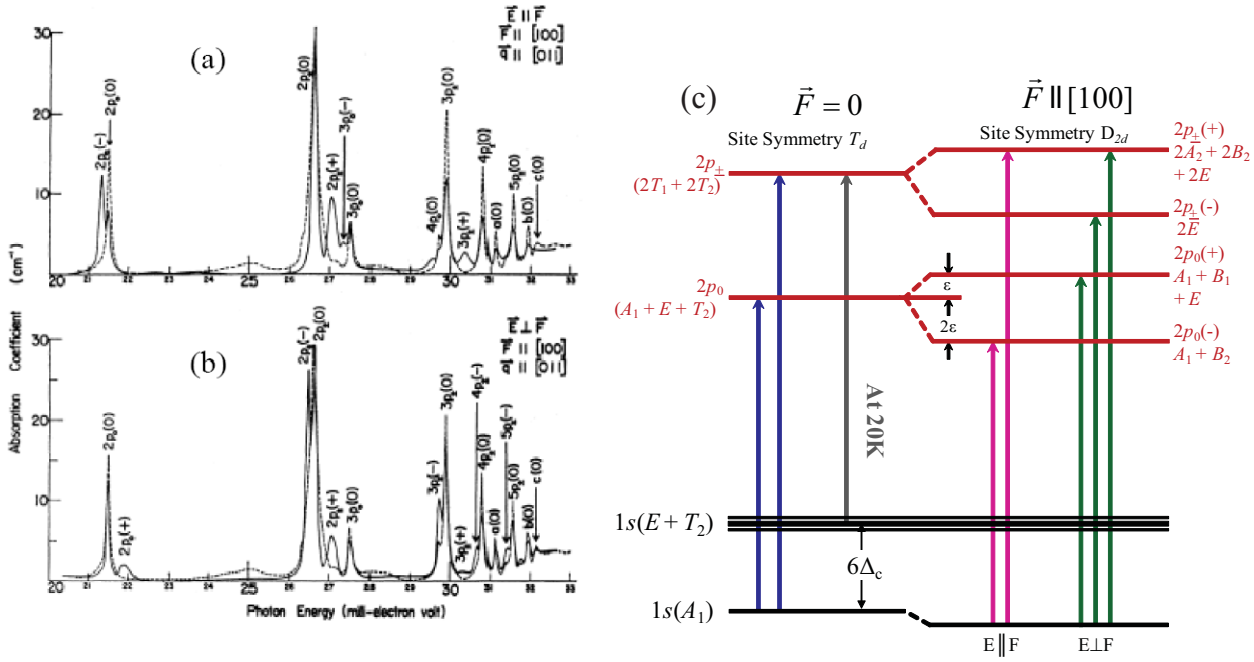

Figure 2.3: The effect of a [100] compression on the excitation spectrum of Li–O center for the direction of light propagation (q) is along [011] for (a) E ∥ F and (b) E ⊥ F. The dashed curves are for F = 0 (c) Splitting of the donor levels in silicon (not to scale) under a [100] compression for a finite $6\Delta_c$. The vertical arrows indicate the allowed transitions. The capital letters labeling the levels denote the irreducible representations of T_d and D_{2d} to which the states belong [27].

2.3 Electron paramagnetic resonance of lithium related centers

2.3.1 Electron paramagnetic resonance of isolated lithium

The electron paramagnetic resonance (EPR) signal of lithium–doped silicon was first observed by Honig *et al.* in a sample containing 7×10^{16} cm^{-3} lithium atoms [74]. The absorption resonance line had the full width at half maximum (FWHM) of 0.15 mT and the isotropic *g*–factor of 1.999 with the line shape being approximately Gaussian. Power saturation characteristics indicate inhomogeneous broadening with four calculated hyperfine lines of 0.01 mT (theoretically estimated) linewidth overlapping and they unresolved in the inhomgeneously

broadened line. This situation was caused by the hyperfine interaction of the Li^0 electron with surrounding ^{29}Si nuclear spins [75, 76].

Watkins studied the orbital degeneracy of the electrons in lithium doped silicon [46]. The EPR and ENDOR spectra were detected by using 10, 14 and 20 GHz frequencies in absorption and dispersion modes. The EPR spectrum of the interstitial isolated lithium (Li^0) under zero stress shows a powder like broad spectrum (Fig. 2.4) that consists of several overlapping lines. This confirms that the ground state is degenerate as in the case of shallow acceptors in silicon [77]. This powder like EPR spectrum was observable in the range of 1.5 – 20 K. The careful observation of the EPR spectrum intensity in the range of 1.5 – 4.2 K revealed that the integrated intensity was roughly constant when corrected for the l/*T* Boltzmann dependence. This behavior confirms that the population distribution of the degenerate ground state is according to the Boltzmann distribution. No significant difference was observed in the EPR spectra between ^6Li and ^7Li doped samples. The *g*–value for the isolated lithium center without external stress was between 1.998 and 1.999.

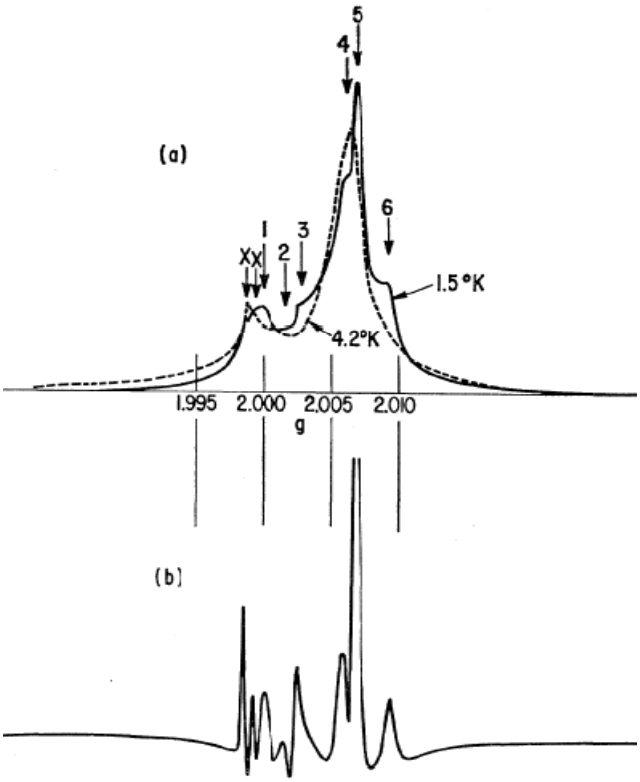

Figure 2.4: EPR spectrum in lithium-doped (~10^{16} cm^{-3}) vacuum floating–zone silicon at zero applied stress, H|| <100>, ν_0 ~20 kMc/sec: (a) absorption at 4.2 and 1.5 K, (b) derivative of dispersion at 1.5 K. [46]

A significant change was observed in the EPR spectrum by the application of compressive uniaxial stress along [100] or tensile stress along [110] directions. As the stress was increased from zero to 10 kg/cm^2, broadening of the resonance spectrum and *g*–shifting towards higher values were observed. At the low stress, strain lifted mixed states are populated according to the Boltzmann factor. This thermal distribution varies by the distribution of strain parameters, because the energy level of 1*s* hydrogenic state of lithium varies as shown in Fig. 2.5. Because dynamic averaging between the ground and excited states occurs [78], for stress more than 10 Kg/cm^2, the EPR spectrum becomes narrower with increasing stress and demonstrates only one EPR absorption line. External stress applied along [00l] and tensile along [011] gives a single sharp line at high stresses, showing the lifting of the degeneracy (Fig. 2.5). This line is described by a tetragonal axial symmetry with the T_{2z} ground state, with *g*–values

$$g_{\parallel} = 1.9997 \pm 0.0001 \text{ and } g_{\perp} = 1.9987 \pm 0.0001.$$

The EPR spectrum of lithium in mechanically damage silicon was intensively studied by Höhne. It was found that the narrow EPR spectrum emerged in the mechanically polished silicon similar to the case of applying uniaxial stress. The mechanical damage in the microregions causes slight deviation in the lithium position near the surface. Indeed it was shown later by Fisher *et al.* that the mechanical polishing of the silicon surface lead to application of an uniaxial stress [79].

At 20 K and $\boldsymbol{B}_0 \parallel$ [100], the observed spectrum can be estimated by the Lorentzian line shape. The spectrum at 1.5 K shows a steep slope at the high–field side towards the middle of the spectrum. This asymmetric line can be explained by Dyson effect [Neu73].

The important features found by the EPR and ENDOR of isolated Li in silicon are as follows:

1) EPR data confirmed that the ground state is 5 fold degenerate and the valley–orbit splitting was inverted from the normal order.

2) In the absence of strain, the ground state is composed of triplet and doublet states splitted by 0.1 – 0.2 cm^{-1} (1 – 2×10^{-5} eV).

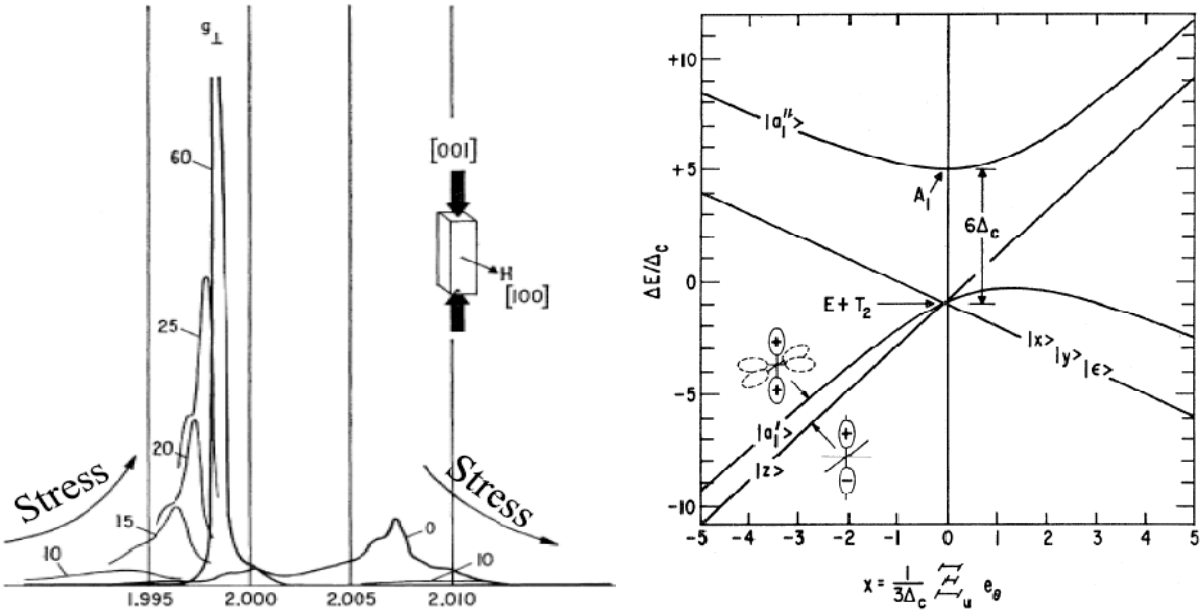

(a) (b)

Figure 2.5: (a) Lithium donor EPR spectrum as a function of [00l] compressive stress (indicated values in kg/cm^2) with H ‖ [l00], ν_0 ~ 20 kMc/sec, and T = 1.5 K. (b) Energy levels of the 1s hydrogenic states of the lithium donor as a function of applied tetragonal strain e_θ[46].

3) A numbers of anisotropic lines were observed below 2.5 K at zero stress and their effective g–values (2.00 – 2.05) are larger than the single line found under stress. The fivefold orbital degeneracy will not be removed by the small stress but these g–values changes significantly by the stress of the order 1 – 10 kg/cm^2.
4) A weak spin–orbit coupling among the T_2 state and between the E and T_2 states are observed with values $|\lambda'| \approx 0.056$ cm^{-1} and $|\lambda| \approx 0.01 - 0.02$ cm^{-1}, respectively. At zero stress the random strain may cause the splitting among the E and T_2 which may be higher than $|\lambda'|$ and $|\lambda|$ but less than $g\beta\boldsymbol{B}_0$.
5) Uniaxial compression or tension removes the fivefold degeneracy of the ground state T_{2z} representing the antisymmetrical combination of valleys on the z axis. The resonance under stress has the axial symmetry about [100] with $g_{\parallel} = 1.9997 \pm 0.0001$ and $g_{\perp} = 1.9987 \pm 0.0001$ that obeys the independent valley model and linewidth 0.13 mT of Li^0 is inhomogeneously broadened by the ^{29}Si hyperfine interaction.

6) The temperature dependence of ^{7}Li and resolved ^{29}Si hyperfine interaction are detected by ENDOR with 470 kg/cm^2 [100] compressive stress and $\boldsymbol{B}_0$ || [100]. It shows that the ^{7}Li hyperfine interaction varies from $A/h \approx 0.01$ MHz at 1.3 K to $A/h \approx 0.1$ MHz at 4 K. The temperature dependence confirms that the T_{2z} is the ground state since the ^{7}Li hyperfine interaction is nearly zero. The small non–zero value of ^{7}Li hyperfine interaction is $A/h \approx 0.004$ MHz when extrapolated to 0 K.

2.3.2 Electron paramagnetic resonance of lithium–oxygen center

Feher observed for the first time an EPR spectrum of Li–O centers in CZ grown silicon of the oxygen content ≈ 10^{17} cm^{-3}. However, the Li–O center was not observed in FZ grown silicon [47] (Fig.2.6). A 9 GHz spectrometer was used to detect Li–O centers and the linewidth along [100] (2.3 ± 0.01 mT) is lower than that in the [110] direction. Therefore this center has the magnetic field direction dependent anisotropy. Later, with 22 GHz (K–band) EPR spectrometer, it was confirmed that two fine structures that had trigonal symmetries with the axial symmetry of the *g*–tensor were pointing along [111] direction. The two principle *g*–values were:

$$g_{\parallel} = g_{[111]} = 1.9978 \pm 0.0001 \text{ and } g_{\perp} = 1.9992 \pm 0.0001.$$

Since the lithium center lies along the [111] direction, an expected ratio of the resolved resonance line intensities are 3:1 and 1:1 in the [111] and [110] directions, respectively. The electron spin lattice relaxation time of Li–O centers at 1.25 K is of the order of 10^2 second that is much shorter than that of phosphorus [28].

The hyperfine interactions (A/h) of the electron wave function with the ^{7}Li and ^{6}Li nuclei are 0.845 MHz and 0.316 MHz, respectively [47, 80]. The hyperfine interaction constant is much smaller than those of other donors in silicon. Figure 2.6 shows the ENDOR signal from ^{7}Li doped silicon (10^{16} cm^{-3}) at temperature 1.25 K and magnetic field along [111] direction. They found two additional structures separated by 0.037 MHz from allowed transition peak positions of ^{7}Li. This additional structure is due to the interaction between the electric field gradient and the quadrupole moment of Li nuclei.

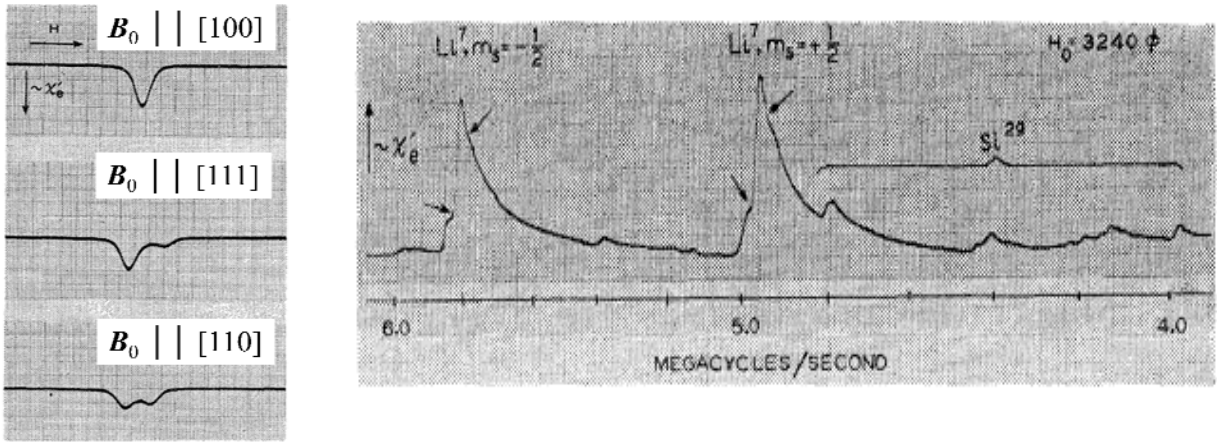

(a) (b)

Figure 2.6: (a) Electron spin resonance signal from Li doped silicon with the magnetic field pointing along the different crystalline directions (~ 3×10^{16} Li/cm^3, T = 1.25 K, ν_e ~ 22700 Mc/sec). The splitting of lines are due to an anisotropic g–value. This indicates that the wave function of the donor electron does not have the tetrahedral symmetry. (b)The ENDOR signals from Li–doped silicon (ν_e ~ 9000 Mc/sec). The additional structure on the ^{7}Li lines is due to a quadrupole interaction.

Chapter 3

Magnetic resonance

3.1 Introduction

Magnetic resonance involves excitation of spins across Zeeman splitted levels. The field has developed as an extension of the Stern–Gerlach experiment [81, 82], which was one of the most famous experiments on the structure of matter in 1920s. It showed that an electron magnetic moment in an atom could take only discrete orientations in a magnetic field. Uhlenbeck and Goudsmit [83] linked the electron magnetic moment with the concept of electron spin angular momentum. The resulting energy of a hydrogen atom in a magnetic field was first studied by Breit and Rabi in 1931 [84]. Later Rabi *et al*. [85] studied the transitions between levels induced by oscillating magnetic field to discover the *magnetic resonance*.

In 1945 an electron paramagnetic resonance (EPR) line was observed for the first time by Zavoisky in a $CuCl_2 \cdot 2H_2O$ sample [86, 87]. The electron spin resonance line was shown at 4.76 mT at radiofrequency of 133 MHz with the electronic *g*–value of approximately 2. Zavoisky's results were interpreted by Frenkel [88] as absorptions due to paramagnetic resonance of electrons. Around the same time, EPR studies were also undertaken in the United States [89] and in England [90]. Two decades later, a high field and high frequency (microwave) EPR spectrometer was developed by Galkin *et al.* [91], since the low field EPR did not provide sufficient spectra separations in certain demanding investigations. The advantage of the use of high frequencies and fields include suppression of the second order effect to simplify the EPR spectra and increase in orientation selectivity and sensitivity. Extensive effort followed to understand the mechanism of EPR theoretically [92, 93].

3.2 Spins behaviors under magnetic field

3.2.1 Semi-classical treatment

Assume that a bar magnet is mounted with a frictionless bearing which could be turned at will. In the presence of time independent magnetic field $\boldsymbol{B}_0$, the bar magnet oscillates about its equilibrium axis. If the bearing was not frictionless, the oscillation damps out and the magnet lies along the magnetic field by giving the energy to the bearing. When the bar magnet has a angular momentum, it acts like a gyroscope.

The equation of motion of the magnet is found by equating the torque with the rate of change of angular momentum $\boldsymbol{J}$.

$$\frac{d\boldsymbol{J}}{dt} = \boldsymbol{\mu} \times \boldsymbol{B}_0 \tag{3.1}$$

where $\boldsymbol{\mu} = \gamma \boldsymbol{J}$. γ is the gyromagnetic ratio.

$$\frac{d\boldsymbol{\mu}}{dt} = \boldsymbol{\mu} \times (\gamma \boldsymbol{B}_0). \tag{3.2}$$

This equation tells us that at any instant the change in $\boldsymbol{\mu}$ are perpendicular to both $\boldsymbol{\mu}$ and $\boldsymbol{B}_0$. As shown in Fig 3.1 and consider that the tail of the vector $\boldsymbol{\mu}$ is fixed and the tip of the vector is moving out of the paper. The angle θ between $\boldsymbol{\mu}$ and $\boldsymbol{B}_0$ does not change and $\boldsymbol{\mu}$ makes a cone. The time derivative of $\boldsymbol{\mu}$ is $\frac{d\boldsymbol{\mu}}{dt} = \frac{\delta\boldsymbol{\mu}}{\delta t} + \omega_0 \times \boldsymbol{\mu}$, we can write equation (3.2) in terms of a coordinate system rotating with arbitrary angular velocity ω_0.

$$\frac{\delta\boldsymbol{\mu}}{\delta t} + \omega_0 \times \boldsymbol{\mu} = \boldsymbol{\mu} \times \gamma \boldsymbol{B}_0$$

$$\frac{\delta\boldsymbol{\mu}}{\delta t} = \boldsymbol{\mu} \times (\gamma \boldsymbol{B}_0 + \omega_0). \tag{3.3}$$

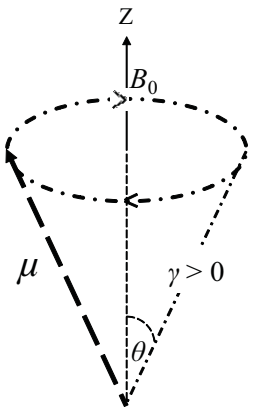

Figure 3.1: Representation of the relation between $\boldsymbol{\mu}$ and $\boldsymbol{B}_0$ for $\gamma > 0$ nuclei. The magnetic moment $\boldsymbol{\mu}$ precesses around a static magnetic field $\boldsymbol{B}_0$ along the *z*–axis.

Equation (3.3) informs that the motion of $\boldsymbol{\mu}$ in the rotating coordinate system obeys the same equation as in the laboratory system, *provided* that it replaces the actual magnetic field $\boldsymbol{B}_0$ by an effective field $\boldsymbol{B}_e$

$$\boldsymbol{B_e} = \boldsymbol{B}_0 + \frac{\omega}{\gamma} \tag{3.4}$$

The motion with respect to the laboratory is therefore that of a vector fixed in a set of axes which themselves rotate at $\omega = -\gamma \boldsymbol{B}_0 k$. In other words, $\boldsymbol{\mu}$ rotates with the angular velocity $\omega = -\gamma \boldsymbol{B}_0 k$ with respect to the laboratory coordinate system. The angular frequency $\gamma \boldsymbol{B}_0$ is called the "*Larmor Frequency*".

3.2.2 Magnetization in a static and oscillating magnetic field

In the absence of magnetic field, the bulk magnetization **M** is zero because the net magnetization is zero. When the ensemble of magnetic moment is exposed to a static and homogeneous magnetic field $\boldsymbol{B}_0$, in the absence of relaxation, **M** is moving according to the equation of motion (3.1)

$$\frac{d\mathbf{M}}{dt} = \gamma \mathbf{M} \times \boldsymbol{B}_0 \tag{3.5}$$

where γ is the electronic or nuclear gyromagnetic ratio equals to $g\beta_{e,n}/\hbar$. Considering $\boldsymbol{B}_0$ along z–axis, equation (3.5) becomes

$$\begin{aligned} \frac{dM_x}{dt} &= \gamma \boldsymbol{B}_0 M_y \\ \frac{dM_y}{dt} &= -\gamma \boldsymbol{B}_0 M_x \\ \frac{dM_z}{dt} &= 0. \end{aligned} \tag{3.6}$$

The solutions of equation (3.6) are

$$\begin{aligned} M_x &= M_\perp^0 cos\omega_{\boldsymbol{B}_0} t \\ M_y &= M_\perp^0 sin\omega_{\boldsymbol{B}_0} t \\ M_z &= M_z^0 \, . \end{aligned} \tag{3.7}$$

Above equations give an idea that **M** precessess about $\boldsymbol{B}_0$ with an angular frequency $\omega_{\boldsymbol{B}_0} = -\gamma \boldsymbol{B}_0$(the classical larmor frequency), if $M_\perp{}^0$ is non–zero. The longitudinal magnetization M_z is constant.

Let us now consider the relaxation effects. When the magnetic field is subjected to sudden changes in its magnitude or direction, then M_x, M_y, and M_z relax to their equilibrium values at different rates. If the static magnetic field suddenly turns on ($\boldsymbol{B}_0 = 0$ at $t = t_0$), then the population difference between the two levels ΔN is governed by the strength of the static magnetic field and temperature obeying the Boltzmaan distribution. Therefore M_z follows an exponential rise with time (Fig. 3.2). The characteristics time at which M_z relaxes to its thermal equilibrium value is defined by longitudinal relaxation time T_1, also called spin lattice relaxation time. The transverse components of magnetization, M_x and M_y, relax with the same rate constants, which are the inverse of a characteristic time T_2 called the transverse relaxation time. Thus

$$\frac{dM_x}{dt} = \gamma \boldsymbol{B}_0 M_y - \frac{M_x}{T_2}$$

$$\frac{dM_y}{dt} = -\gamma \boldsymbol{B}_0 M_x - \frac{M_y}{T_2} \tag{3.8}$$

$$\frac{dM_z}{dt} = \frac{M_z^0 - M_z}{T_1}.$$

The above equations are known as Bloch equations [94]. The solution of these empirical equations feature the decay of the components M_x and M_y to zero. Note that both T_1 and T_2 are empirical bulk properties. Now we consider the effect of the oscillating magnetic field on the each component of the magnetization.

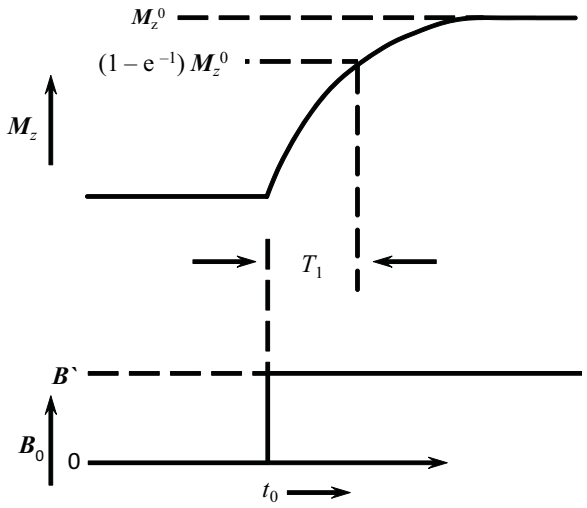

Figure 3.2: Behavior of the magnetization M_z when a magnetic field $\boldsymbol{B}_0$ lying along z–axis is abruptly increased from zero to a magnitude $\boldsymbol{B}`$ at time $t = t_0$. T_1 is the longitudinal relaxation time.

The transition can be induced between the two magnetic–energy levels when an oscillating magnetic field ($\boldsymbol{B}_1$) is introduced perpendicular to the static magnetic field ($\boldsymbol{B}_0$). A sinusoidally varying monochromatic field $\boldsymbol{B}_1$ is introduced with components

$$B_{1x} = B_1 \cos \omega t$$

$$B_{1y} = B_1 \sin \omega t \tag{3.9}$$

$$B_{1z} = 0.$$

With the addition of the terms for these components, the complete equations of the motion are

$$\frac{dM_x}{dt} = \gamma(B_0 M_y - B_1 \sin \omega t M_z) - \frac{M_x}{T_2}$$

$$\frac{dM_y}{dt} = -\gamma(B_1 \cos \omega t M_z - B_0 M_x - \frac{M_y}{T_2} \tag{3.10}$$

$$\frac{dM_z}{dt} = \gamma(B_1 \sin \omega t M_x - B_1 \cos \omega t M_y) + \frac{M_z^0 - M_z}{T_1},$$

where ω represents the component along the z–axis. ω may be a positive or negative. One alternating component rotates in the same direction as the magnetic moment precession and another component precesses in the opposite direction. Here the anticlockwise component is neglected. Because **M** is continuously precessing about $\boldsymbol{B}_0$, it is easier to visualize the time dependence of **M** if we switch to a rotating frame coordinate. The components of **M** in the rotating frame are given by $M_{x\phi}$, $M_{x\phi}$, and M_z. The Bloch equations in the rotating frame are;

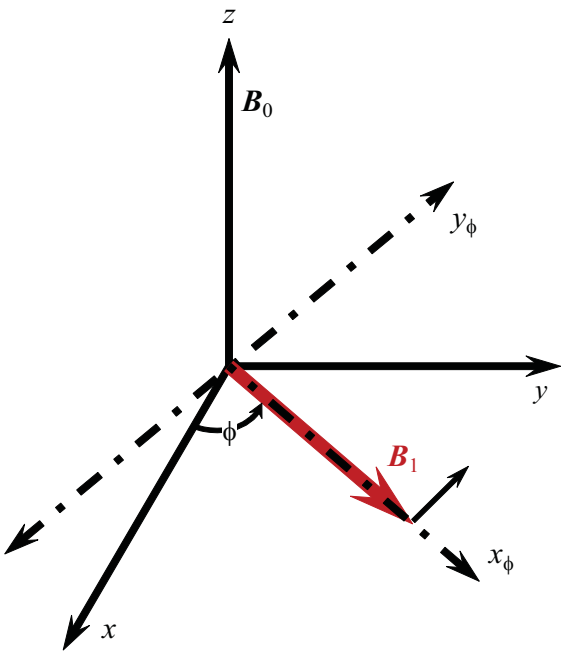

Figure 3.3: Diagram showing the rotating frame (dashed lines) in relation to an axis system fixed in space. This frame rotates at an angular frequency ω with the same sense as the rotation of $\boldsymbol{B}_1$.

$$\frac{dM_{x\phi}}{dt} = -\left(\omega_{B_0} - \omega\right)M_{y\phi} - \frac{M_{x\phi}}{T_2}$$

$$\frac{dM_{y\phi}}{dt} = \left(\omega_{B_0} - \omega\right)M_{x\phi} + \gamma B_1 M_z - \frac{M_{y\phi}}{T_2} \qquad (3.11)$$

$$\frac{dM_z}{dt} = -\gamma B_1 M_{y\phi} - \frac{M_z - M_z^0}{T_1}.$$

3.2.3 Steady state solution of the Bloch equation

Equation (3.11) is a set of coupled linear differential equations with constant coefficients. The steady–state solutions are;

$$M_{x\phi} = -M_z^0 \frac{\gamma B_1(\omega_{\boldsymbol{B}_0} - \omega)T_2^2}{1+(\omega_{\boldsymbol{B}_0} - \omega)^2 T_2^2 + \gamma^2 \boldsymbol{B}_1^2 T_1 T_2}$$

$$M_{y\phi} = +M_z^0 \frac{\gamma \boldsymbol{B}_1 T_2}{1+(\omega_{\boldsymbol{B}_0} - \omega)^2 T_2^2 + \gamma^2 \boldsymbol{B}_1^2 T_1 T_2} \qquad (3.12)$$

$$M_z = +M_z^0 \frac{1 + (\omega_{\boldsymbol{B}_0} - \omega)^2 T_2^2}{1+(\omega_{\boldsymbol{B}_0} - \omega)^2 T_2^2 + \gamma^2 \boldsymbol{B}_1^2 T_1 T_2}.$$

Note that the response $M_{x\phi}$ is in phase with $\boldsymbol{B}_1$, whereas $M_{y\phi}$ is 90˚ out of phase. The magnitudes of $M_{x\phi}$ and $M_{y\phi}$ tend to be small compared to that of M_z^0. For sufficiently small values of $\boldsymbol{B}_1$, the term in each denominator may be neglected. This power–saturation term predicts that **M** vanishes as $\boldsymbol{B}_1$ increases. Note that only the half of the radiation–energy density is effective in inducing transitions. The effects of the oscillating field $\boldsymbol{B}_1$ are often described in terms of dynamic susceptibilities χ' and χ'' (often called the "Bloch susceptibilities"). The magnetization **M** is related to the applied magnetic field $\boldsymbol{B}_0$ by a dimensionless proportionality factor χ with the relations

$$\mathbf{M} = \chi\mathbf{H} = \chi\boldsymbol{B}_0/\kappa\mu_0 \tag{3.13}$$

$$M_z^0 = \chi^0\boldsymbol{B}_0/\kappa\mu_0 = \tfrac{1}{2}\gamma\beta\Delta N/V \tag{3.14}$$

where μ_0, κ and ΔN are the permeability, the relative permeability and steady state population. χ^0 is the static magnetic susceptibility $\kappa\mu_0 N_v g^2\beta^2/4k_bT$. Here N_v is the number of spins in the total sample volume v and β is the Bohr magneton. χ and κ are isotropic. Then, with equations (3.13) and (3.14), we can define dynamic susceptibilities via

$$\chi' = \kappa\mu_0 M_{x\phi}/B_1$$

$$\chi'' = -\kappa\mu_0 M_{y\phi}/B_1 \tag{3.15}$$

where B_1 is the half the amplitude of the linearly polarized excitation field. Thus

$$\chi' = \chi^0 \frac{\omega_{B_0}(\omega_{B_0}-\omega)T_2^2}{1+(\omega_{B_0}-\omega)^2T_2^2+\gamma^2B_1^2T_1T_2}$$

$$\chi'' = \chi^0 \frac{\omega_{B_0}T_2}{1+(\omega_{B_0}-\omega)^2T_2^2+\gamma^2B_1^2T_1T_2}\,. \tag{3.16}$$

Note that $\chi'' = \chi'/[(\omega_B - \omega)T_2]$ depends on $\boldsymbol{B}_0$, and $\boldsymbol{B}_1$. Figure 3.4 illustrates the frequency profile of χ' and χ'' under non–saturating conditions. Equation (3.10) are not correct for small static field $\boldsymbol{B}_0$ (i.e., $\boldsymbol{B}_0 \leq \boldsymbol{B}_1$) since the susceptibilities do not vanish at $\omega_B = 0$. The power $P_a(\omega)$ absorption of the linearly polarized excitation field by the magnetic system (equation (3.9)) is

$$P_a(\omega) = \frac{\omega\chi''B_1^2}{\mu_0 V} \tag{3.17}$$

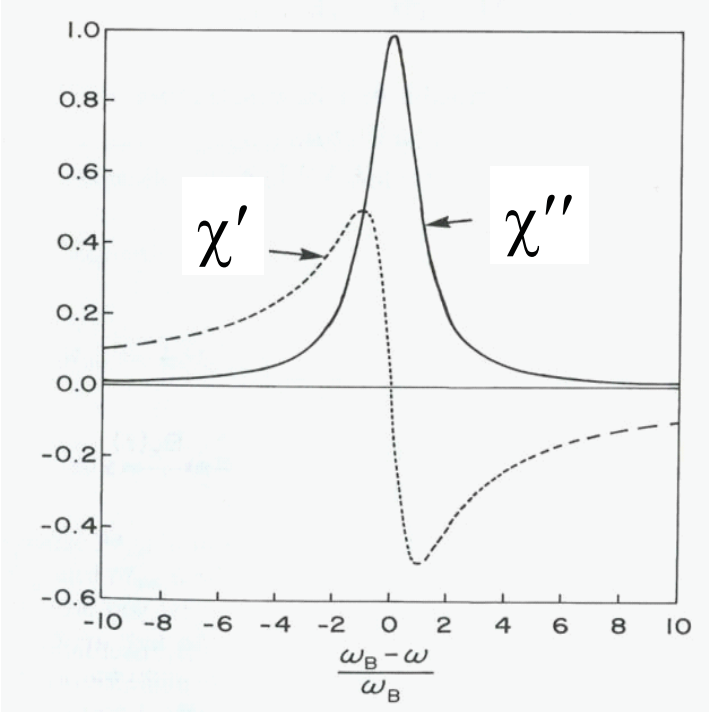

Figure 3.4: In-phase (χ') and out – of – phase (χ'') components of dynamic magnetic susceptibilities versus the angular frequency deviation [95].

3.3 Spin–spin interaction

The presence of a group of spins ($\boldsymbol{S} = ½$ or $\boldsymbol{I} \geq ½$) around one particular spin may result in a number of interactions. The most important interaction between the spin and the surrounding spins is the dipolar interaction, contact hyperfine interaction, exchange interaction, and quadrupolar interaction. When the dipolar interaction dominates between the nuclear spins and nuclear and electron spins, the linewidth of nuclear magnetic resonance and electron paramagnetic resonance broaden, respectively. The contact interaction between donor electron wave functions and nuclear spins are often referred to as the contact hyperfine interaction. The contact hyperfine interaction between the electrons and ^{29}Si nuclei is responsible for the ^{29}Si nuclear *spin–lattice relaxation* mechanism [96]. When the donor concentration is more than 10^{17} cm^{-3}, it causes a significant electron wave function overlaps. Therefore the exchange interaction

occurs. Quadrupole interaction becomes relevant when the nuclear spin is greater than ½. The interaction between the electric field gradient and quadrupole moment leads to emergence of forbidden transitions.

3.3.1 Dipolar interaction

Classically, the dipolar interaction energy depends on the relative orientation of the magnetic moments. Consider a case that two magnetic dipoles, μ_1 and μ_2, are placed at an angle θ, and at a distance r as shown in Fig. 3.5. This is the case between ^{29}Si nuclei and electron spins in a strong magnetic field. The interaction energy E between the two magnetic moments is

$$E = \frac{\mu_1 \mu_2}{r^3} - \frac{3(\mu_1.r)(\mu_2.r)}{r^5}. \tag{3.18}$$

μ_1 and μ_2 are considered as operators in the quantum mechanical treatment. Substitution of $\gamma_i \hbar \boldsymbol{I}_i$ into μ_i makes the Hamiltonian in the form;

$$\mathcal{H}_d = \frac{\hbar^2 \gamma_1 \gamma_2}{r^3}\left[I_1.I_2 - \frac{3(I_1.r)(I_2.r)}{r^2}\right]. \tag{3.19}$$

In the spherical coordinate system the Hamiltonian becomes,

$$\mathcal{H}_d = \frac{\hbar^2 \gamma_1 \gamma_2}{r^3}[A + B + C + D + E + F] \tag{3.20}$$

where,

$$A = I_{1z} I_{2z}(1 - 3cos^2\theta)$$

$$B = -\frac{1}{4}(I_1^+ I_2^- + I_1^- I_2^+)(1 - 3cos^2\theta)$$

$$C = -\frac{3}{2}(I_1^+ I_{2z} + I_{1z} I_2^+)sin\theta cos\theta e^{-i\varphi}$$

$$D = -\frac{3}{2}(I_1^- I_{2z} + I_{1z} I_2^-)sin\theta cos\theta e^{-i\varphi}$$

$$E = -\frac{3}{4}(I_1^+ I_2^+)sin^2\theta e^{-2i\varphi}$$

$$F = -\frac{3}{4}(I_1^- I_2^-)sin^2\theta e^{2i\varphi}$$

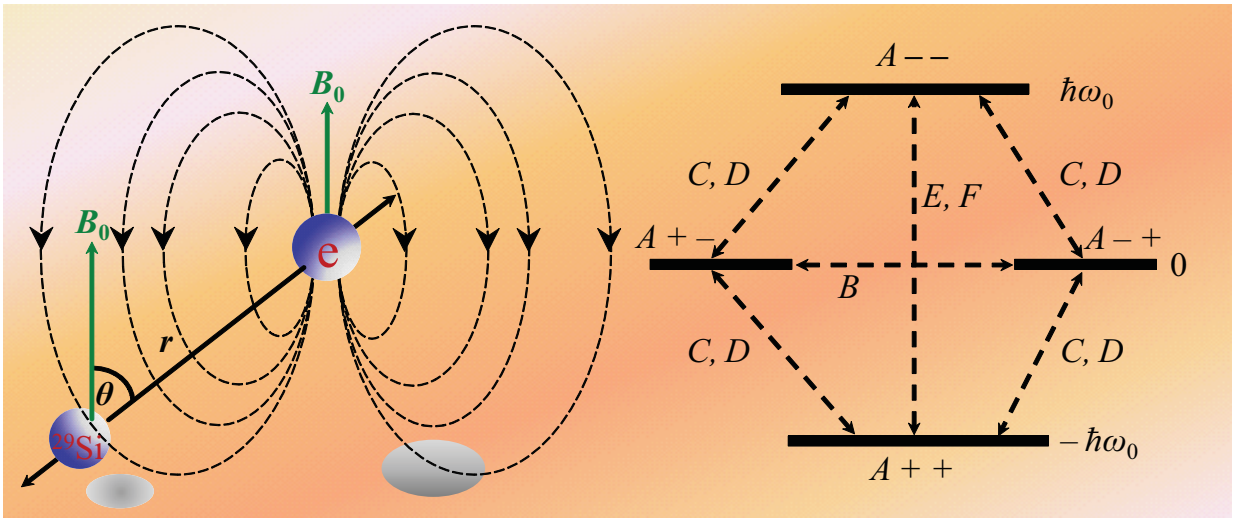

(a) (b)

Figure 3.5: (a) Schematic representation of the dipolar interaction between two spins. A vector joining the spins at a distance r makes an angle θ with static magnetic field $\boldsymbol{B}_0$. (b) The energy level diagram for the two identical spins. The Zeeman Hamiltonian $\mathcal{H}_z = \gamma\hbar\boldsymbol{B}_0\boldsymbol{I}_{2z}$ corresponds to interaction with static magnetic field $\boldsymbol{B}_0$. The dashed lines joining the states show the matrix elements.

where $I^+ = I_x + iI_y$ and $I^- = I_x - iI_y$ are the rising and lowering operators, respectively, that satisfy the commutation relations $[I_z, I^\pm] = \pm I^\pm$ $[I^+, I^-] = 2I_z$.

To understand the meaning of the term $A - F$, we shall consider a simple example of one $\boldsymbol{I} = ½$ nuclear spin interacting with one $\boldsymbol{S} = ½$ electron spin. It is convenient to denote the state $m_1 = +½$, and $m_2 = -½$ by notation $|+ -\rangle$. The energy level diagram and matrix elements connecting them are shown in Fig. 3.5 (b). $I_{1z}I_{2z}$ is proportional to the term A that is a diagonal term. This

means it connects the same energy levels ($|m_1 m_2\rangle$ with $\langle m_1 m_2|$). On the other hand the term *B* causes simultaneous flips of the two spins because of the term $I_1^+ I_2^- + I_1^- I_2^+$. In view of the fact that the terms *C* and *D* each flips one spin only, they join the states differ by the energy $\hbar\omega_0$. The terms *E* and *F* connect states differ by the energy $2\hbar\omega_0$. The terms *B*, *E* and *F* are responsible for forbidden transitions in EPR, i.e. flip–flop and flip–flip transitions. Such forbidden transitions play important roles in the dynamic nuclear polarization of ^{29}Si nuclear spins by lithium EPR (sec. 5. 2. 2).

Sum of the terms *A* and *B* gives what it is called $\mathcal{H}_d^0$:

$$\mathcal{H}_d^0 = \frac{1}{2}\frac{\gamma^2\hbar^2}{r^3}(1 - 3cos^2\theta)(3I_{1z}I_{2z} - I_1.I_2) \tag{3.21}$$

It is important to note that certain values of $\mathcal{H}_d^0$ are positive (magnetic energy increasing) and certain values of $\mathcal{H}_d^0$ are negative (magnetic energy decreasing). The term involving the ($3cos^2\theta$ – 1) in equation (3.21) is of particular importance. For a fixed value of *r*, this term causes the interaction energy to dependent highly on the angle θ. However the value of this term vanishes when $cos^2\theta$ = 1/3, i.e., θ = 54° and 144°. For these particular angles, the dipolar interaction disappears even when the spins are close to each other in space. They are called "*magic angles"* and employed frequently in NMR to suppress the dipolar broadenings. Such a measurement is known as the "*magic angle spinning*".

3.3.2 Contact hyperfine interaction

The contact interaction arises when wave functions of two objects overlap in space. The most important cases are overlaps between electron and nuclear spins and between electron and electron spins.

The contact interaction between electron and nucleus spins is known as the *Fermi contact interaction***.** The Fermi contact interaction is also called donor hyperfine interaction. The total spin Hamiltonian between one electron spin and one donor nuclear spin is given by

$$\widehat{\mathcal{H}} = g\beta_e \boldsymbol{B}_0 \hat{S} - g_n \beta_n \boldsymbol{B}_0 \hat{I} + A_0 \hat{I}\hat{S} \,. \tag{3.22}$$

The term A_0 is called the isotropic hyperfine coupling constant

$$A_0 = \frac{8\pi}{3} \hbar \gamma_e \gamma_n |\psi(0)|^2, \tag{3.23}$$

where $\hbar$, $\gamma_{e,n}$ and $|\psi(0)|^2$ are the reduced Planck's constant, gyromagnetic ratio of electron and nuclear spins, and the donor wave function amplitude at the donor center, respectively. The ionization energies, hyperfine line splitting [97, 98], and the values of the wave function amplitude at the impurity center are summarized in Table 3.1 for donors in silicon [99].

Lithium has the lowest ionization energy with the ground state T_{2z}. Since the ground state T_{2z} has the p character, the contact hyperfine interaction becomes very small leading to a very narrow EPR lines.

Table 3.1: Experimental values of the ionization energy, nuclear magnetons[a)], the hyperfine line separations, and theoretical estimation of $|\psi(0)|^2$ for different donors in silicon.

Donor	Ionization Energy (meV)	Nuclear Magneton (μ/μ_N)	ΔH (mT)	$\lvert\psi(0)\rvert^2$ (10^{24} cm^{-3})
^{7}Li	33	3.25	0.0036	1.7
^{31}P	44	1.13	4.2	44
^{75}As	49	1.5	22.8	110
^{121}Sb	39	3.4	34.5	110

[a)] Nuclear magnetic moment in units of the nuclear magneton μ_N

3.3.3 Exchange interaction

The exchange interaction is a non–classical effect. It occurs when wave functions of two or more identical particles overlap. It results in either increase or decrease in the expectation values of the energy. Discussions of the terms that contribute to the exchange interaction are beyond the scope of this work but can be found in [MS80]. In general the spin exchange interaction is given by

$$\mathcal{H}_{ex} = S_1^T J_0 S_2 \tag{3.25}$$

where J_0 = tr(**J**)/3 is the isotropic electron–exchange coupling constant. When the lithium donor concentration in silicon is higher than 10^{17} cm^{-3}, the lithium donor wave functions overlap. At such a high concentration, the hopping conduction delocalizes the electrons. However the lithium samples employed in this study are in the range of 10^{16} cm^{-3} and the exchange interaction becomes least important.

3.3.4 Quadrupolar interaction

The quadrupolar interaction, referred to as the quadrupolar coupling, exists only for nuclear spins with $\boldsymbol{I} > ½$. A nucleus with $\boldsymbol{I} > ½$ has a non–spherical charge distribution, and the electric quadrupole moment of the nucleus interacts strongly with the electric field gradients generated by the surrounding electrons. This is called quadrupole interaction. The electron spin resonance spectrum show (2$\boldsymbol{S}$) (2$\boldsymbol{I}$ + 1) number of peaks, when the crystal field is negligible and the external filed is parallel to the symmetry axis. Otherwise many forbidden lines are observed. The selection rule states that transitions $|M, m\rangle \leftrightarrows |M–1, m–1\rangle$ and $|M, m–1\rangle \leftrightarrows |M–1, m\rangle$ are forbidden. Since lithium has two stable isotopes, ^{6}Li (I = 1) and ^{7}Li (I = 3/2), it is possible to observe 4 and 2, (6 and 4) forbidden lines for ^{6}Li (^{7}Li) nuclei for the condition $\Delta m = \pm 1$ and $\Delta m = \pm 2$, respectively. This interaction leads to the appearance of the forbidden EPR transition peaks as shown in Fig 3.6 [100].

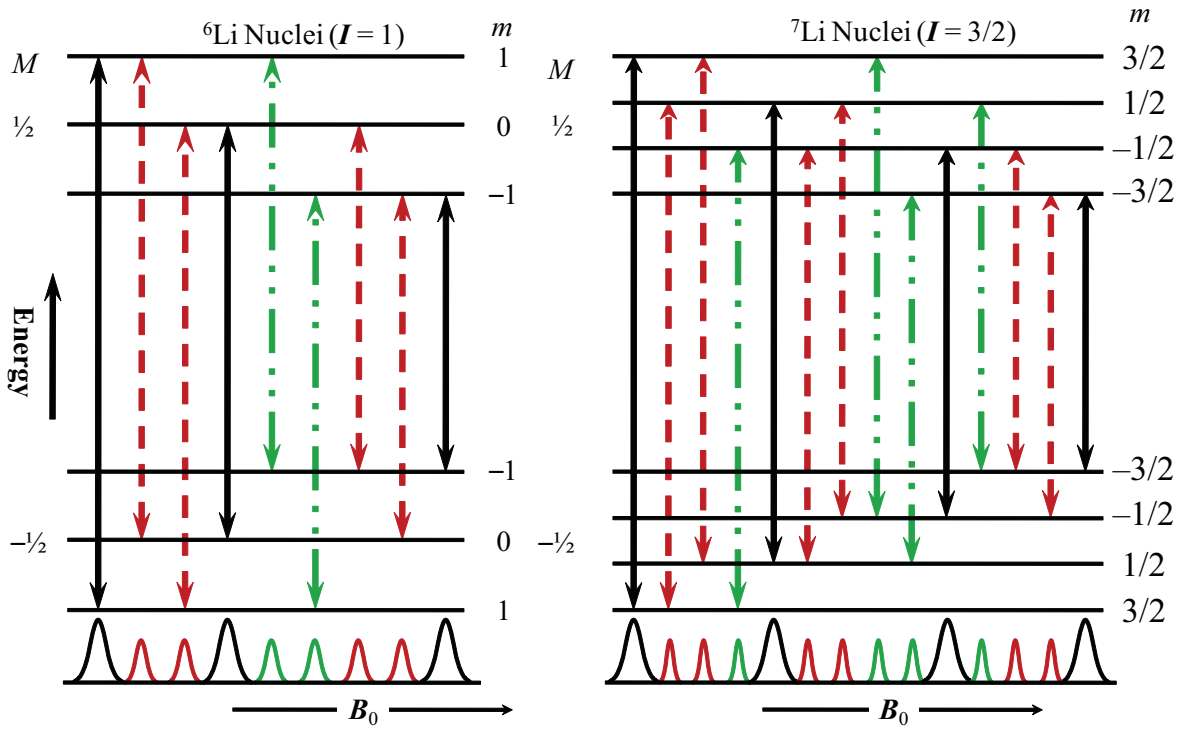

Figure 3.6: Schematic representations of the energy level diagram for the M (1/2 ⇆ –1/2) interacting with ^{6}Li ($\boldsymbol{I}$ = 1) and ^{6}Li ($\boldsymbol{I}$ = 3/2) nuclei donors in silicon. The possible number and relative positions of allowed, [$\Delta M = \pm 1$ (black line)] and forbidden hyperfine transition, [$\Delta m = \pm 1$ (red dashed line) and $\Delta m = \pm 2$ (green dashed line)] are shown.

Chapter 4

Electron paramagnetic resonance of lithium related centers in isotopically controlled silicon

4.1 Electron paramagnetic resonance and spin lattice relaxation

This chapter investigates the symmetry of lithium related centers using an EPR spectrometer. When a single $\boldsymbol{S}$ = ½ electron spin is concerned, the interaction between the electron spin magnetic moment with the magnetic field $\boldsymbol{B}_0$, lifts the degeneracy and splits the level into two with the magnetic quantum number m_s = + ½ and m_s = – ½, corresponding to spin up and spin down, respectively, as shown in Fig. (4.1). Population of the two spin states m_s = ½ and m_s = –½ are represented by N_+ and N_-, respectively. The population difference between the states is $\Delta N = N_+ - N_-$.

$$N_+ = ½ (N - \Delta N)$$

$$N_- = ½ (N + \Delta N) \qquad (4.1)$$

where N is the total number of spins.

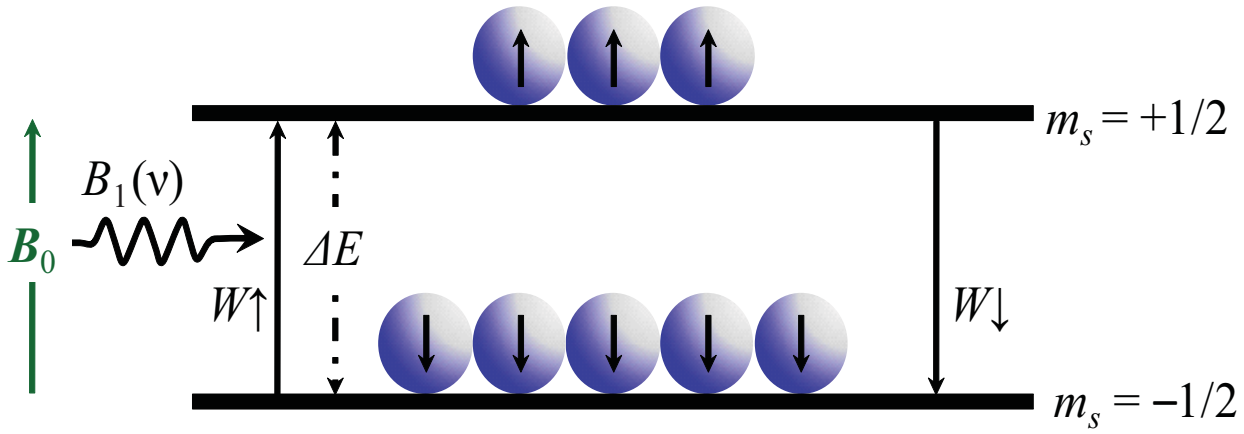

Figure 4.1: Two level spin system at temperature T and magnetic field $\boldsymbol{B}_0$. $N_{½}$ and $N_{-½}$ are the number of spins occupying the upper and lower energy levels, respectively. W↑ and W↓ are the transition probabilities per unit time for upward and downward transitions, respectively, ΔE is the energy separation of the two levels, and $\boldsymbol{B}_1$ is the excitation field amplitude with the frequency ν.

Since it has been assumed that the spins are isolated from each other, the rate equation for this kinetics system is,

$$\frac{d\Delta N}{dt} = -2N\_W\uparrow + 2N\_W\downarrow \tag{4.2}$$

where W↑ and W↓ are the transition probability per unit time for upward and downward transitions respectively.

The first and second terms on the right side are the rate of upward and downward transitions, respectively. The factor 2 appears because one upward or downward transition changes ΔN by 2. The equation (4.2) can be rewritten as

$$\frac{d\Delta N}{dt} = N(W\downarrow - W\uparrow) - \Delta N(W\downarrow + W\uparrow)$$

$$= \left(N\frac{W\downarrow - W\uparrow}{W\downarrow + W\uparrow} - \Delta N\right)(W\downarrow + W\uparrow)\,. \tag{4.3}$$

Under the steady state $\left(\frac{d\Delta N}{dt} = 0\right)$, we obtain,

$$\Delta N^{ss} = N_{+}{}^{ss} - N_{-}{}^{ss}$$

$$= N\frac{W\downarrow - W\uparrow}{W\downarrow + W\uparrow}$$

$$\frac{d\Delta N}{dt} = (\Delta N^{ss} - \Delta N)(W\downarrow + W\uparrow) \tag{4.4}$$

where ΔN^{ss} is the steady state population difference. The quantity $(W\downarrow + W\uparrow)^{-1}$ has a dimension of time and is known as the relaxation time T_1. Thus, the equation (4.4) becomes

$$\frac{d\Delta N}{dt} = \frac{N^{ss} - \Delta N}{T_1}$$

$$\Delta N = N^{ss}(1 - e^{-t/T_1}) \tag{4.5}$$

By combining the rate equations for a transition induced by the applied alternative field $\boldsymbol{B}_1(\nu)$ in the thermal equilibrium process, we find

$$\frac{d\Delta N}{dt} = -2WN^{ss} + \frac{N^{ss} - \Delta N}{T_1} \tag{4.6}$$

where W is the mean transition probability per unit time induced by field $\boldsymbol{B}_1(\nu)$ between the states $m_s = +\,½$ and $m_s = -\,½$. The mean transition probability is proportional to the square of the alternating magnetic field ($W \propto \boldsymbol{B}_1{}^2$). The steady state of equation (4.6) is

$$\Delta N = \frac{N^{ss}}{1+2WT_1}. \tag{4.7}$$

Therefore as long as $2WT_1 << 1$, $\Delta N = N^{ss}$ and the absorption of energy from the alternating field does not disturb the population much from their thermal equilibrium value. The rate of absorption energy is given by

$$\frac{dE}{dt} = \Delta N \hbar \omega W = N^{SS} \hbar \omega \frac{W}{1 + 2WT_1}. \quad (4.8)$$

The absorption rate by the electron increases with increasing the alternating magnetic field amplitude as long as $2WT_1 << 1$. When $W \sim \frac{1}{2}T_1$, there is a limiting point of power at which the ability of the sample to dissipate energy from its spin to its lattice saturate. This behavior is regarded as the saturation of spin system. These considerations lead to the following expression for the electron spin–lattice relaxation rate constant:

$$T_1 = \frac{1}{2T_2 \gamma_e^2 \boldsymbol{B}_1^2}. \quad (4.9)$$

4.2 Electron paramagnetic resonance of lithium related centers

4.2.1 Sample preparation

A *n*–type FZ naturally abundant silicon (4.7% ^{29}Si nuclei) sample and a isotopically enriched ^{28}Si sample with ^{28}Si concentration 99.991% grown along <100> direction and having the resistivity of 2000 Ωcm were used for the lithium diffusion. Prior to the lithium diffusion, the silicon wafers were mechanically polished using rotary polisher (model no: ML150P) with the 1900 mesh slurry. The polishing was done in three different rotation speeds 150, 120 and 60 rpm. Polishing with the 1900 mesh size creates the roughness of order of 10–100 μm. This rough surface helps the evaporated lithium atoms to stick more effectively to the silicon surface.

Lithium diffusion was performed at *UC Berkeley* using a thermal evaporator equipped with in–situ diffusion annealing capability. A heater is attached to the top of the sample holder as shown in the Fig. 4.2. To prevent the oxidation of lithium pallet, it was kept immersed in the oil and put inside the thermal evaporator just before evacuation of the thermal evaporator. Lithium evaporation was done at 10^{-6} mbar. The sample holder was heated just after evaporation of lithium. The sample holder is heated till its temperature reached 450ºC and the temperature was kept constant at the same level for 15 min with the assumption that sample and sample holder have the same temperature. After the lithium diffusion, the sample is immediately quenched in

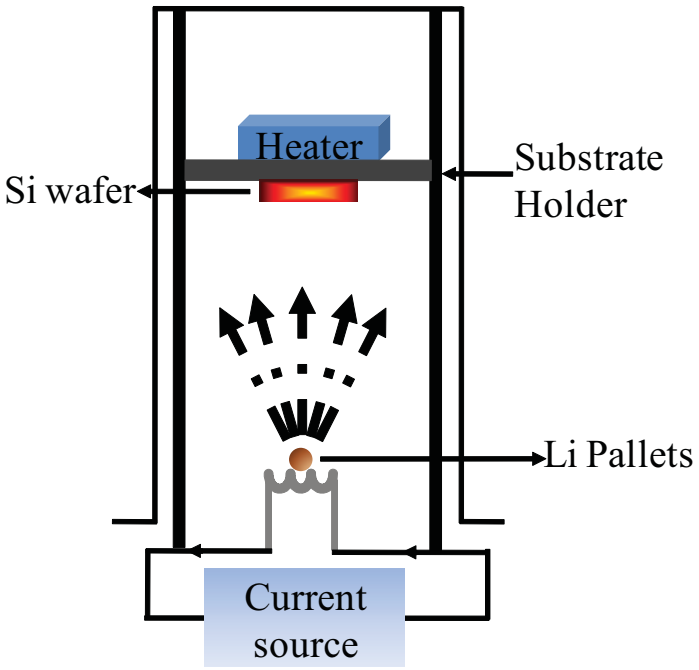

Figure 4.2: Schematic diagram of the thermal evaporator. The evaporation of lithium is done at 10^{-6} mbar vacuum.

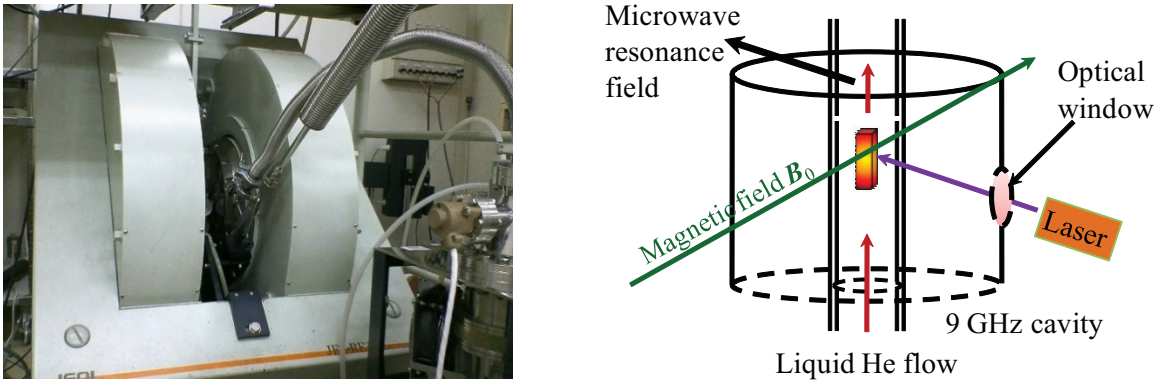

(a) (b)

Figure 4.3: (a) An X–band JOEL JES–RE3X ESR spectrometer equipped with a cylindrical cavity. (b) Schematic diagram of Oxford ER4118CF He gas flow cryostat.

an ethanol bath to prevent immediate formation of Li–O complexes. This lithium diffused silicon sample was labeled as Si:Li^0. Part of the lithium diffused silicon wafer was put inside the ampoule and sealed with the vacuum up to 10^{-5} mbar. The ampoule sealed silicon sample was annealed at 450ºC for 45 min in an electric furnace. By this annealing lithium–oxygen complexes were formed. Such a sample was labeled as Si:Li–O.

Both the lithium diffused and annealed silicon samples were etched by a $HF:HNO_3$ = 1:3 solution for 2 min to remove the surface damage prior to the EPR measurement. Two X–band EPR spectrometers were employed; JEOL, JES–RE3X and Bruker E500. An Oxford He gas flow cryostat was used to control the sample temperature in the range of 3.4 – 50 K. Figure 4.3 show the EPR spectrometer and the schematic diagram of the Oxford He gas flow cryostat.

4.2.2 EPR spectra in naturally abundant silicon

Second derivative line shape of EPR absorption spectra observed in silicon after diffusion of Li atoms at 450^{o}C for 15 min are shown in Fig. 4.4 (a). This sample is labeled as ^{nat}Si:Li^0. The angular dependence of this EPR spectrum (Fig. 4.4 (b)) shows an axially symmetric *g*–tensor about <100> with the components $g_{\|} = g_{[100]} = 1.9996 \pm 0.0001$ and $g_{\perp} = 1.9986 \pm 0.0001$, which are in good agreement with the previously reported values for neutral Li atoms (Li^0) occupying tetrahedral interstitial positions [46]. It should be noted that the EPR spectra shown in Fig. 4.4 (a) are recorded without application of external stress that was needed to obtain such spectra in the earlier studies [46]. The existence of uniaxial stress in the direction perpendicular to the silicon surface after mechanical grinding was demonstrated previously [79, 78 and 101]. However, we observe the signal shown in Fig. 4.4 (a) even after sufficient chemical etching of the surfaces to remove such stress. The possible reason for this spectrum is due to some residual stress exist perpendicular to [100] direction even after chemical polishing in bulk crystal or better crystal which removes the degeneracy of ground state of lithium atom. This signal can be detected at temperatures below 20 K and its intensity continues to increase all the way down to 3.4 K, which was the lowest temperature employed in this study.

Isolated lithium shows considerably narrower linewidth of 0.05–0.13 mT in naturally abundant silicon. The theoretical calculation performed by Kohn shows that the linewidth $\langle \Delta H^2 \rangle^{1/2}$ depends proportionally to the $n^{-3/2}$, where n is the square root of the ratio of the effective–mass binding energy (29 meV) and actual Li binding energy (33 meV) [31]. This effect itself reduces the resonance linewidth by a factor of 0.8 than other donors. Moreover, since the ground state of lithium wave function has the p–character, the hyperfine interaction is surpressed. Therefore, the EPR linewidth of Li is very sharp.

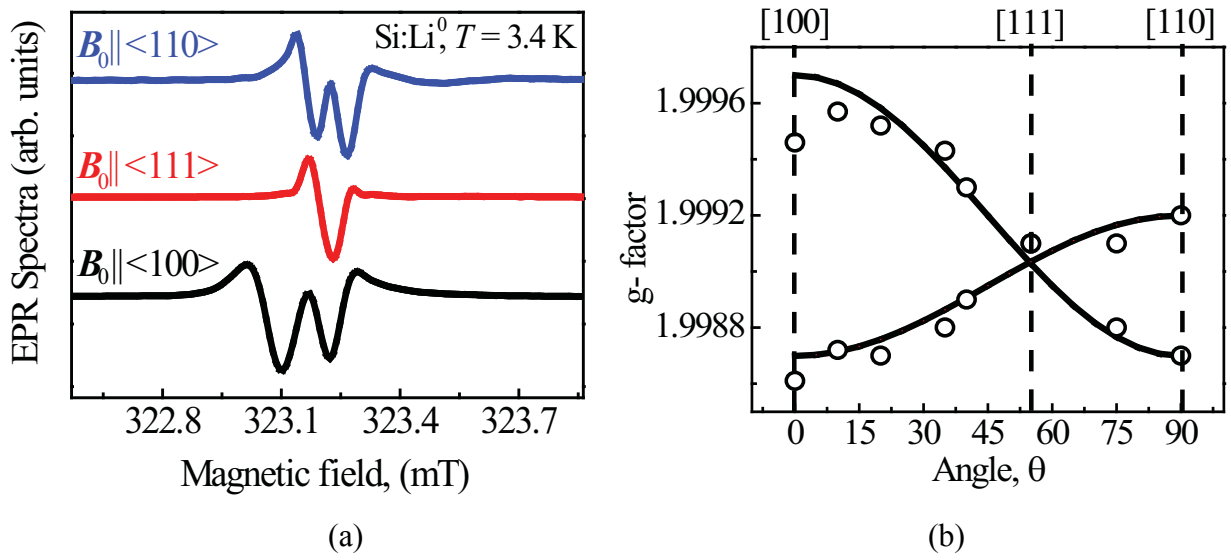

Figure 4.4: (a) EPR spectra of Li^0 center detected in the second derivative mode with different orientation of magnetic field $\boldsymbol{B}_0$ indicated in the Figure. (b) The angular dependence of EPR signals position where θ is the angle between the symmetry axis <100> and applied magnetic field direction.

An additional EPR lines emerge in the Li diffused samples immediately after annealing at 450ºC for 45 min labeled (I) in Fig. 4.5 (a). Moreover, these EPR centers are not stable at room temperature and change their character over the time period of days and are labeled (II) and (III) in Fig. 4.5 (a). One broad and stable peak labeled (III) is observed and that is used for further analysis for symmetry consideration. The variation of this broad line at different orientations of the crystal in the magnetic field agrees with those indentified as Li–O center [68] and marked as

^{nat}Si:Li–O. The angular dependence of ^{nat}Si:Li–O EPR spectrum (Fig. 4.5 (b)) shows trigonal symmetry (C_{3v}) with an axially symmetric *g*–tensor about <111> with the components $g_{\|} = g_{[111]}$ =1.9979±0.0001 and $g_{\perp}$=1.9990±0.0001.

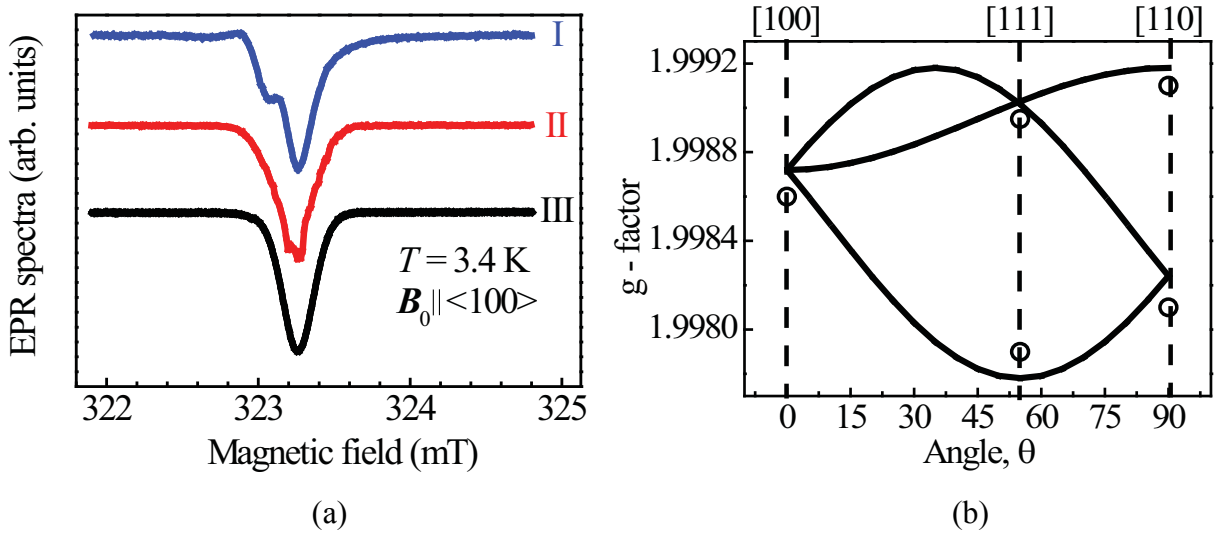

Figure 4.5: (a) EPR spectra detected in the second derivative of absorption mode: (I) immediately after 45 min annealing at 450°C, (II) after two days, and (III) after 4 weeks. The peak (III) arises from Li–O center. (b) The angular dependence of ^{nat}Si:Li–O center signal position where θ is the angle between symmetry axis <111> and applied magnetic field direction.

The variation of the EPR spectra with the time after the second annealing can be related to slow relaxation of lattice stress in the sample and, probably, to slow but mobile Li even at room temperature after the second annealing. Li atoms may tend to stabilize themselves near interstitial oxygen to form Li–O centers. The concentration of paramagnetic Li–O centers estimated from the EPR line intensities in comparison with the reference sample (Si:P concentration 10^{16} cm^{-3}) is around 2×10^{16} cm^{-3} which is below the typical concentration 5×10^{16} cm^{-3} of oxygen in FZ silicon.

4.2.3 Temperature and power dependence of EPR spectra

Figure 4.6 shows the temperature and power dependences of the EPR signal amplitudes for different samples (^{nat}Si:Li^0 and ^{nat}Si:Li–O). Below 10 K, the EPR intensity of the isolated Li increases whereas that of Li–O centers decreases. The temperature dependence of the Li–O EPR intensity decreases below 10 K, and is explained by longer electron spin–lattice relaxation time (T_{1e}) than that for Li^0 centers [28]. T_{1e} time of Li–O center is 100 sec at 1.25 K [47], whereas Li^0 center is 12 μsec at 2.1 K [SPT$^+$08]. Dependence of the peak–to–peak first derivative amplitude on microwave power is shown in Fig. 4.6 (b). High microwave power is required in case of isolated lithium (Li^0) compared to Li–O center because of its short relaxation time T_{1e}. This can be understood by equation (4.9) which shows that saturation power is limited by the relaxation time.

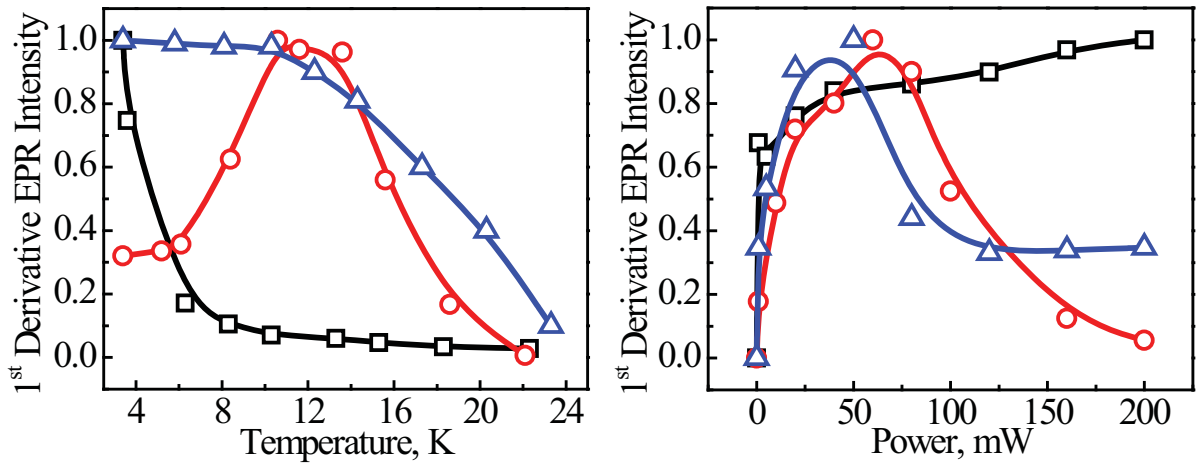

Figure 4.6: The dependences of the EPR line amplitudes on the (a) temperature and (b) power of samples containing Li^0 (□) and Li–O (○) centers in dark and under illumination for Li–O center (△).

The saturation behavior of EPR spectrum in all investigated samples shows that EPR spectrum is inhomogeneously broadened. Inhomogeneous broadening is due to presence of background ^{29}Si in naturally abundant silicon. To overcome this effect it is preferred to use isotopically controlled silicon.

4.2.4 EPR spectra of lithium related center in ^{28}Si isotopically enrich silicon

We observe significant narrowing in isolated lithium EPR spectrum in ^{28}Si:Li^0 sample. The angular dependence and temperature dependence of EPR spectrum are similar to those observed in ^{nat}Si:Li^0 sample as shown in Fig. 4.4 (b) and Fig. 4.6 (a). The intensity of Li^0 EPR spectrum decreases under illumination. The second derivative EPR linewidth of Li^0 detected along different crystalline orientations in ^{28}Si:Li^0 sample was only ~ 0.025 mT. Figure 4.7 shows the comparison between the EPR spectrum of ^{nat}Si:Li^0 and ^{28}Si:Li^0 which is significantly narrower than 0.05 – 0.13 mT found for ^{nat}Si:Li^0. No hyperfine structure of Li^0 in ^{28}Si:Li^0 was observed. Since the ground state of Li^0 is not a singlet lithium donor electron wave function at the nucleus $|\psi'(0)|^2 \simeq 0.002 \times 10^{24}$ cm^{-3} is 250 times smaller than that of phosphorus [97]. The previous ENDOR investigation found that the hyperfine interaction $A(^7\text{Li})$ for Li^0 varied with temperature from 0.07 MHz at 3 K to 0.1 MHz at 4 K corresponding to hyperfine splitting from 0.0025 to 0.0036 mT, respectively [46]. Such hyperfine splitting was not detectable in the present study since it was at least one order of magnitude smaller than the EPR linewidth. The linewidth comparison for the Li^0 and Li–O centers in naturally abundant silicon and ^{28}Si isotopically enriched silicon is listed in Table 4.1.

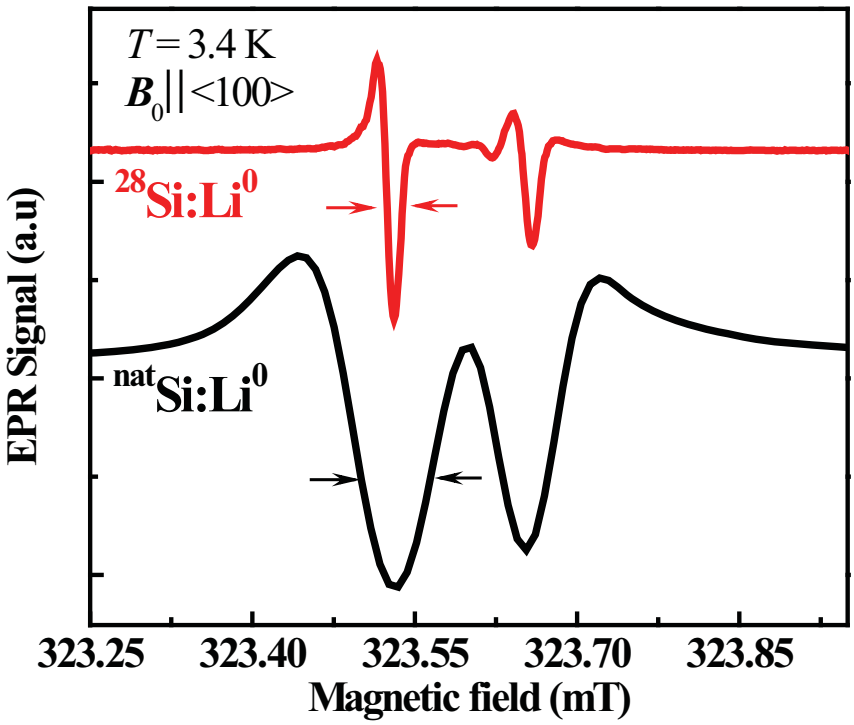

Figure 4.7: EPR spectra of the Li^0 center in $^{nat}Si:Li^0$ (black line) and $^{28}Si:Li^0$ (red line) for $B_0 \parallel$ [100]. The spectrum was detected in the second derivative mode at 3.2 K, with ν_e = 9.0512 GHz and microwave power = 12 μW.

In the temperature range 8 – 14 K, another EPR signal of "trigonal symmetry" attributed to Li–O center [47] with well resolved ^{7}Li hyperfine structure is observed in $^{28}Si:Li^0$. The maximum Li–O EPR intensity in dark is achieved around 10 – 12 K. At lower temperatures, due to the increase of the spin lattice relaxation time with decreasing temperature (up to 10^2 sec below 3.1 K [47]), Li–O EPR intensity decreases in dark. Here illumination of above band gap light is found to be effective in decreasing the spin lattice relaxation time due to spin exchange between the photoexcited conduction electrons and donor electrons leads to enhance the EPR signal [103, 104] in combination with the low microwave power (~ 12μW) to avoid the saturation of the EPR transition. The Li–O EPR spectra detected in $^{28}Si:Li–O$ and $^{nat}Si:Li–O$ are shown in Fig. 4.8 to illustrate the striking difference between these two. The spectrum detected on $^{28}Si:Li–O$ sample show significant reduction in inhomogeneous broadening to show the hyperfine structures similar to the case of EPR of $^{28}Si:P$ and $^{28}Si:B$ [105, 106].

Table 4.1: Li^0 and Li–O linewidths of the naturally abundant silicon and ^{28}Si isotopically enriched silicon.

Donor	Linewidth (mT)
$^{nat}Si:Li^0$	0.13
$^{28}Si:Li^0$	0.025
$^{nat}Si:Li–O$	0.23
$^{28}Si:Li–O$	0.03

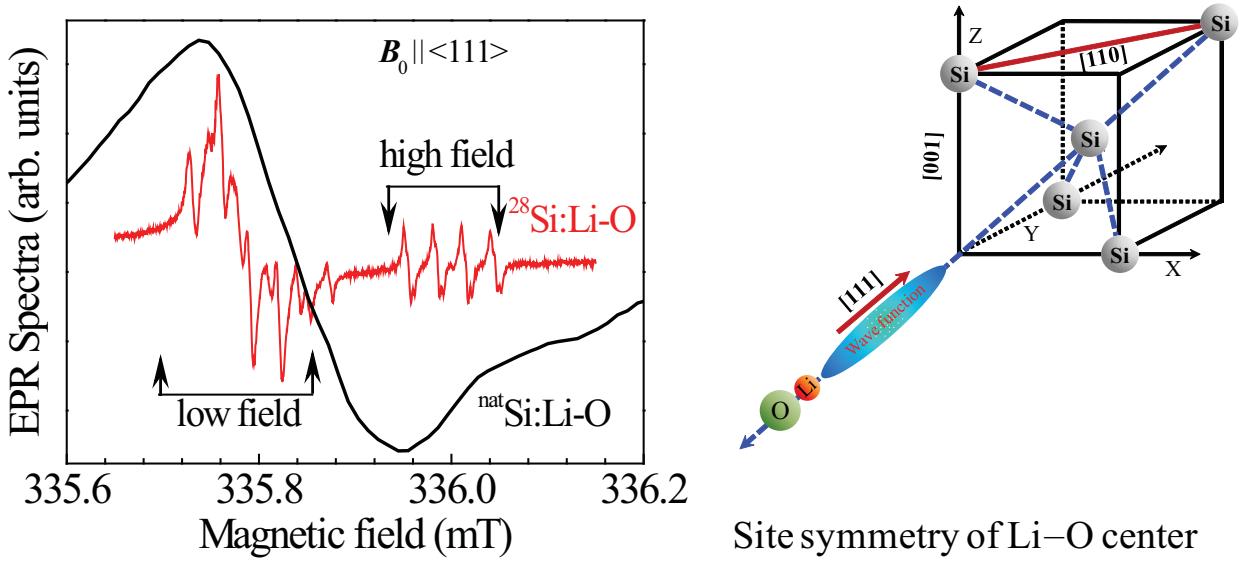

(a) (b)

Figure 4.8: (a) The Li–O EPR spectra recorded with $^{28}Si:Li^0$ and $^{nat}Si:Li–O$ under illumination at 4.2 K, $\boldsymbol{B}_0$ ||<111>, and ν_e= 9.3973 GHz. The low–field group is composed of twelve overlapping ^7Li hyperfine structures oriented along three equivalent directions along <111> that are not parallel to $\boldsymbol{B}_0$. The high–field group is composed of four ^7Li hyperfine structures originating from the centers oriented along one of four <111> directions parallel to $\boldsymbol{B}_0$. (b) Four red balls along <111> crystallographic directions represent microstructure of Li–O complexes due to ^7Li or ^6Li isotopes.

Li–O hyperfine interaction due to the ^{7}Li isotope (nuclear spin I = 3/2, natural abundance 92.41%) is $A(^7\text{Li})$ = 0.845 MHz [80, 47] corresponding to splitting of ~0.03 mT. This splitting is isotropic within our experimental error leading to the appearance of four equidistant hyperfine lines marked as high–field in Fig. 4.8. The four lines appear by the usual relation $2I$+1 of the Li–O centers oriented along one of the four equivalent <111> orientations that are parallel to the direction of $\boldsymbol{B}_0$ as shown in Fig. 4.8. The EPR signal marked as low–field in Fig. 4.8 consists of twelve overlapping lines due to the slight misorientation of the sample with respect to the $\boldsymbol{B}_0$ direction employed in the EPR measurements. Otherwise four hyperfine lines would have been expected.

4.3 Monoclinic symmetry of Li–O centers

Figure 4.9 shows unexpected splitting of the high–field group of four lines at different angles of magnetic field directions around the <111> axis. The weak line in the center of spectrum shown in Fig. 4.9 originates from the hyperfine structure due to the ^{6}Li isotope (spin I=1, abundance 7.59%). This splitting cannot be explained by misorientation of the sample and/or interaction of the ^{7}Li nuclei quadrupole moment with the gradient of the electric field because such effects do not lead to appearance of the forbidden EPR transition peaks at the energy lower than the lowest energy allowed transition nor after the highest energy allowed transition [107]. Therefore, reasonable explanation of the splitting of the high–filed EPR lines under rotation is the symmetry the centers being lower than trigonal symmetry. The possible reason for lower symmetry of Li–O center is the displacement of lithium nuclei from [111] crystal axis due to the interaction between two ^{7}Li nuclei or lattice distortion due to formation of Li–O complex at interstitial site.

The angular dependence of the g–factors for the high–field part of EPR spectra is shown in Fig. 4.10. Solid lines are the calculated angular dependences with ~3^o deviation of axial symmetry axis from the [111] crystal axis towards [011] in the $(1\bar{1}0)$ plane with g_1=g_2=1.9994 and g_3=1.9978. These g–tensor component values are close to those determined in Reference [47]. It corresponds to the monoclinic symmetry of the g–tensor having the principal axis g_1 along $[1\bar{1}0]$, angle $\theta \approx 58^o$ between g_3 axis and [001] direction, and orthogonality $g_2 \perp g_1$, g_3 [108]. Such

symmetry describes experimentally observed splitting of the EPR lines by two components with the intensity ratio 1:2 when B_0 is exactly in the {110} plane and by three components with equal intensities under small misorientation of the sample. Within the experimental accuracy these parameters describe very well the positions of all EPR lines recorded at B||<100> and B||<110>.

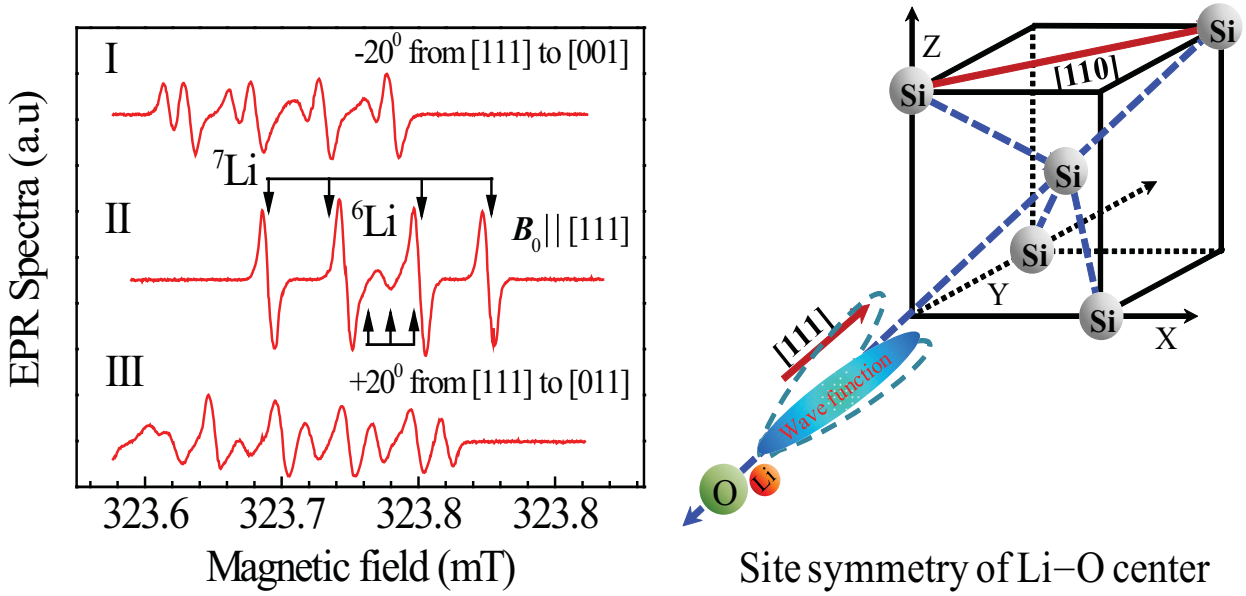

(a) (b)

Figure 4.9: (a) The high–filed group of EPR spectra detected under illumination at 4.2 K of ^{28}Si:Li–O in three different orientations (I) $\boldsymbol{B}_0$ along –20° from [111] towards [001] (II) $\boldsymbol{B}_0$ along [111] (III) $\boldsymbol{B}_0$ along +20° from [111] towards [011]. T = 4.2 K and ν_e = 9.0512 GHz. The high-field group of lines consists of hyperfine due to ^{7}Li (4 lines) and ^{6}Li (3 lines) isotopes. (b) Schematic representation of 3 degree misorientation of the Li–O center from <111> towards [011] crystallographic plane.

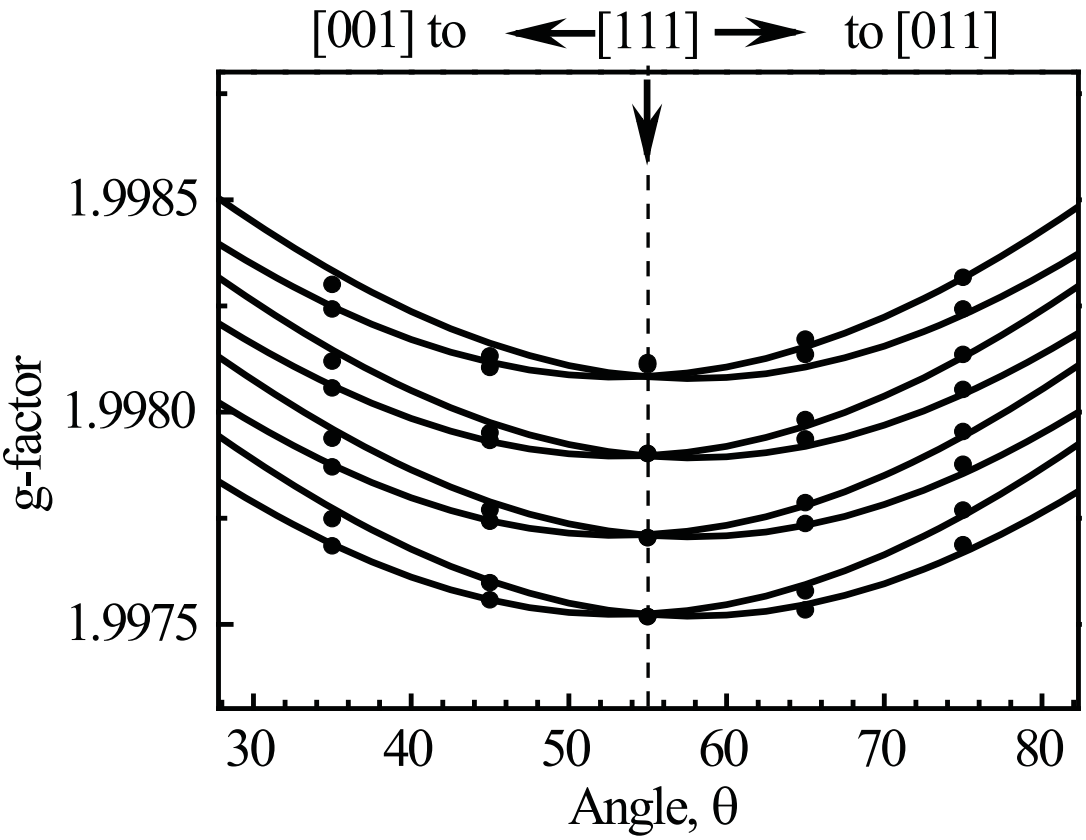

Figure 4.10: The angular dependence of the Li–O *g*–factors recorded with ^{28}Si:Li–O under illumination at 4.2 K. Solid lines are the fitting of the experimental points (•) as described in the text.

Additional structure in the Li–O EPR signal was found in ^{28}Si:Li^{0} at temperatures below 4 K with B_0||<111> and under illumination (Fig. 4.11). Each of four high–field ^{7}Li hyperfine EPR lines has four additional components spaced by 0.004 mT. The structures become much more complicated for other B_0 directions due to the increasing number of lines reflecting the monoclinic symmetry. Such additional structure with four lines can arise from the hyperfine interaction with other distant ^{7}Li nuclei. However, an additional structure observed in the ^{7}Li ENDOR spectrum was reported by G. Feher attributed to the quadrupole interaction [47 and 107]. Further investigations are needed to identify the origin of this structure.

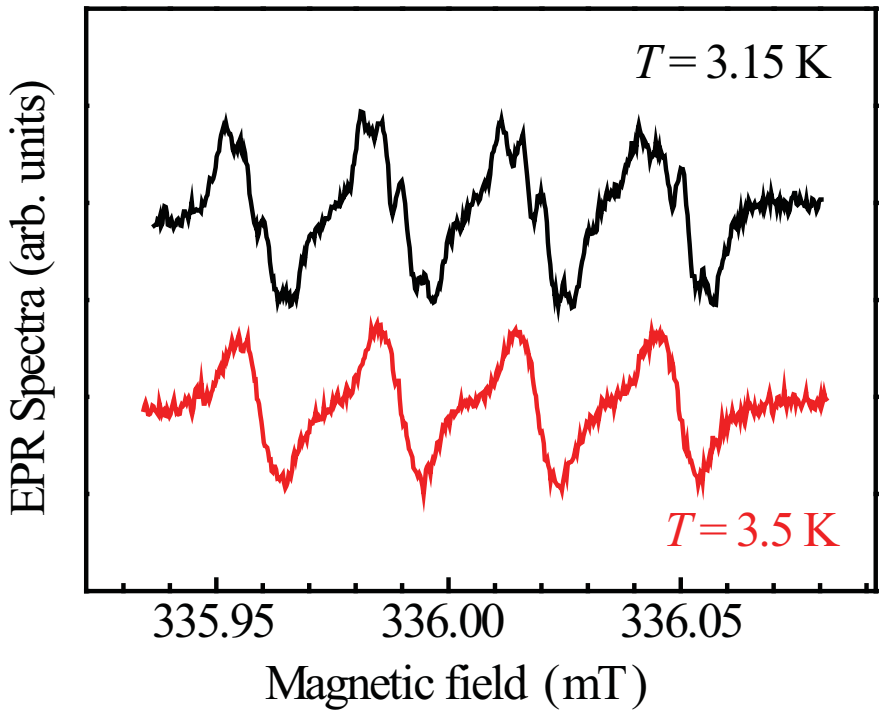

Figure 4.11 An additional structure appearing among each ^{7}Li hyperfine line with the equal spacing of 0.004mT only for temperatures below 3.5 K. Here $\boldsymbol{B}_0$||<111>, microwave field power =12 μW, and ν_e =9.39526 GHz. The spectrum taken at 3.15 K shows such additional structures while that taken at 3.5 K doesn't.

4.4 Summary

The EPR spectrum of the Li related donor center in FZ Si was observed at T = 3.4 – 20 K implying that Li^0 has a shorter electron spin lattice relaxation time than that of phosphorus. Isotope enrichment of the silicon host single crystal with the nuclear-spin-free ^{28}Si stable isotope removed the inhomogeneous broadening of EPR lines originating from isolated interstitial lithium (Li^0) donors and lithium-oxygen (Li–O) complex centers. The hyperfine structures normally hidden by inhomogeneous broadening are made visible. Analysis of such hyperfine structures reveals that the g-tensor of the Li–O complexes exhibits the monoclinic symmetry. At temperatures below 3.5 K, additional splitting of the ^{7}Li EPR lines of Li–O is observed.

Chapter 5

Dynamic nuclear polarization of ^{29}Si nuclei induced by Li and Li–O centers in silicon

5.1 Dynamic nuclear orientation

5.1.1 Nuclear orientation

Consider an assembly of identical nuclei in which each is characterized by an angular momentum $\boldsymbol{I}\hbar$ and associated with the magnetic moment $\vec{M} = \hbar\gamma\vec{I}$, where $\hbar$ and γ are the reduced Planck's constant and the nuclear gyromagnetic ratio, respectively. Gyromagnetic ratio is either positive or negative depending on the nature of nuclei and inversely proportional to the nuclear mass.

Suppose a simple case, when a nucleus with nuclear spin I = ½ and positive gyromagnetic ratio is placed in an external magnetic field $\boldsymbol{B}_0$ along the z–axis. For this system there exist $2I + 1 = 2$ eigenstates. The nuclear magnetic moment always couples with the external magnetic field with the energy called eigenvalue E_m. This eigenvalue E_m is known as the Zeeman energy and given by

$$E_m = -\overrightarrow{M_m} . \overrightarrow{B_0} . \tag{5.1}$$

Figure 5.1 shows the energy levels diagram of $\boldsymbol{I}$ = ½ spins under external magnetic field at temperature T. The number N_+ and N_- represent the "spin up" and "spin down" populations of the quantum states, respectively. Boltzmann statistics determines the population among the eigenstates which is proportional to exp $(-E_m/k_BT)$, where k_BT is the thermal energy. The thermal equilibrium polarization can be given by the following equation

$$P_n = \frac{N_+ - N_-}{N_+ + N_-} = tanh(g\beta B_0/2kT) \tag{5.2}$$

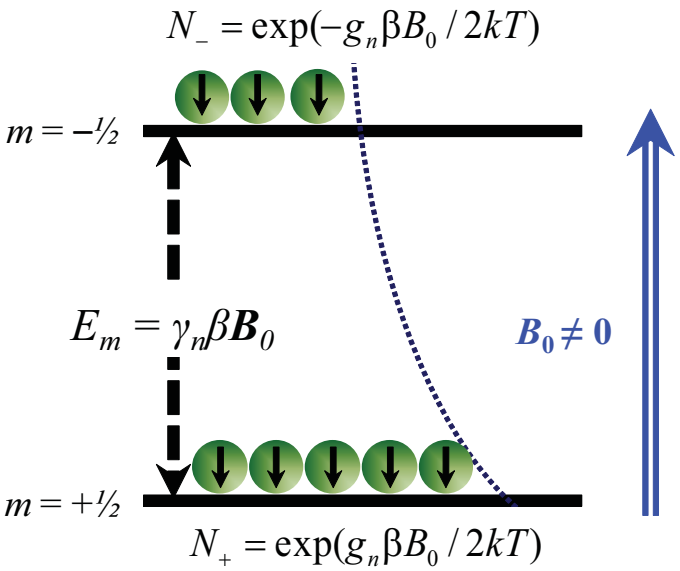

Figure 5.1: Energy levels and occupations at $\boldsymbol{I}$ = ½ spin states in a static magnetic field $\boldsymbol{B}_0$ and constant temperature T. For $\boldsymbol{B}_0 > 0$, the thermal equilibrium polarization is tanh $(g\beta\boldsymbol{B}_0/2kT)$.

The nuclear polarization at room temperature and 7 T are typically of the order of 10^{-5} to 10^{-7}. Such low polarization is due to the thermal energy being much larger than the Zeeman energy. Thus appreciable polarization can be obtained only for very large field and very low temperature by this "brute force" method. However even with the use of available NMR in market at 21 T and liq. He temperature (4.2 K), the maximum polarization of ^{29}Si nuclei can reach 10^{-4}. However this is not sufficient for the application of quantum computers and spintronics.

An above mentioned method is known as the static equilibrium method [109, 110]. In late 1950s, Overhauser [111], Jeffries [112], and Abragam [113 and 114] showed an efficient method for the

polarization of nuclei. The dynamic nuclei polarization (DNP) of the ^{29}Si nuclei was demonstrated for the first time by Abragam in silicon doped with phosphorus $N(\mathrm{P}) \approx 5\times10^{16}$ cm^{-3} [115]. The DNP enhancement (E) of 30 corresponding to a nuclear polarization (P_n) of 0.048 % was observed under saturation of the phosphorus electron paramagnetic resonance (EPR) lines by microwave field at 4.2 K [115]. Much lower DNP enhancement of E = 4.6 was observed in similar silicon crystals at 6 K but a large enhancement E = 511 corresponding to ^{29}Si nuclei polarization 0.28 % was achieved at 12 K in an naturally abundant silicon crystal (4.7% ^{29}Si nuclei) with the phosphorus concentration 10^{16} cm^{-3} [29, 30]. To achieve higher DNP degrees, it is prefer to saturate the EPR transition at low temperatures. However long electron spin–lattice relaxation time of phosphorus limits ^{29}Si nuclei to polarize at low temperatures. The short electron spin–lattice relaxation time of lithium related centers give a prospect to polarize the ^{29}Si nuclei at low temperature. Therefore, we investigate the dynamic nuclear polarization of ^{29}Si nuclei due to lithium related centers in silicon. There are several mechanisms for DNP, among them *solid effect* phenomena were observed in all investigated sample. For this reason I will discuss the *solid effect* mechanism in the next section.

5.1.2 Solid effect

A magnetically dilute solid containing N electron spin ($\boldsymbol{S}$ = ½) and n nuclear spin ($\boldsymbol{I}$ = ½) is placed in a microwave cavity at magnetic field $\boldsymbol{B}_0$ and low temperature T. This system is represented by the energy level diagram in Fig. 5.2 and eigenstates are labeled by the zero order magnetic quantum number $|M, m\rangle$. The eigenstate energy levels are shown in Fig. 5.2, where $\Omega = g\beta B_0/kT$ and $\Sigma = g_n\beta B_0/kT$ are the electron spin and nuclear spin thermal equilibrium polarizations, respectively. The spin Hamiltonian for the entire sample can be expressed as

$$\mathcal{H} = g\beta \sum_l \boldsymbol{B}_0 . S_l - g_n\beta \sum_m \boldsymbol{B}_0 . I_m + \sum_{m.l} V_{ml} + \sum_{m>n} U_{mn} \qquad (5.3)$$

where $\boldsymbol{S}_l$ and $\boldsymbol{I}_m$ are the lth electron and mth nuclei, respectively in the lattice. The terms in equation (5.3) represent the electron Zeeman, nuclear Zeeman, electron–nuclear and nuclear–nuclear interaction, respectively. Since the sample consisting of dilute electron spins ½ ($N << n$)

quadrupole interaction and electron–electron interaction are neglected. The third term contains the contact and dipole–dipole interactions. Therefore, the *Hamiltonian* for the third term is;

$$V_{ml} = I_m \,.\, A_{ml} \,.\, S_l - \frac{\gamma_e \gamma_n \beta^2}{r_{ml}^3}\left[I_m . S_l - \frac{3(I_m . r_{ml})(S_l . r_{lm})}{r_{lm}^2}\right] \tag{5.4}$$

where r_{lm} is the displacement vector between $\boldsymbol{I}_m$ and $\boldsymbol{S}_l$ and $\boldsymbol{A}_{lm}$ are the tensor. For a convenience, consider only single pair of $\boldsymbol{I}_m$,$\boldsymbol{S}_l$ and assume that the first term of equation (5.4) is negligible. Therefore dipole coupling between $\boldsymbol{I}_m$ and $\boldsymbol{S}_l$ plays an significant role for this system. The second term includes operator products of the form $I_{\pm}.S_{\pm}$ and $I_{\pm}.S_{\mp}$ (see equation (3.20)) which allow for the admix of the zero–order states and allow for additional transitions of type I_z, $S_z \rightarrow I_z \pm 1$, $S_z \pm 1$ (flip–flip transition) and I_z, $S_z \rightarrow I_z \pm 1$, $S_z \mp 1$ (flip–flop transition), respectively. Therefore the forbidden transition allows us to flip the nuclear spin under microwave irradiation. To realize this process, it is needed to consider the relaxation rate of the each process under microwave irradiation.

The effective relaxation in this system under the microwave irradiation field corresponds to the transition $\Delta M = 1$, $\Delta m = 0$ i.e., electron spin flips only. This rate is α_1 per sec. The *flip–flop* ($\Delta M = 1$, $\Delta m = -1$) and *flip–flip* ($\Delta M = 1$, $\Delta m = 1$) relaxation rates are α_2 and α_3, respectively. The forbidden transition relaxation rate is slower than electron spin flip transition rate α_1 by a factor σ.

$$\sigma = \frac{3}{10}\left(\frac{\gamma_e \beta}{r^3 H}\right)^2 . \tag{5.5}$$

Nuclear spin relaxation ($\Delta M = 0$, $\Delta m = 1$) occurs at rate α_4. In general at low temperature (4.2 K) nuclear spin relaxation rate is three orders slower than α_1. Both α_2 and α_3 represent the flipping of nuclear spins through the electron spin flipping.

The thermal equilibrium population in column (I) is according to equation (5.2) leading to the static nuclear polarization

$$P_0 = \tanh(\Sigma/2) \approx h\nu_n/2kT \,. \tag{5.2}$$

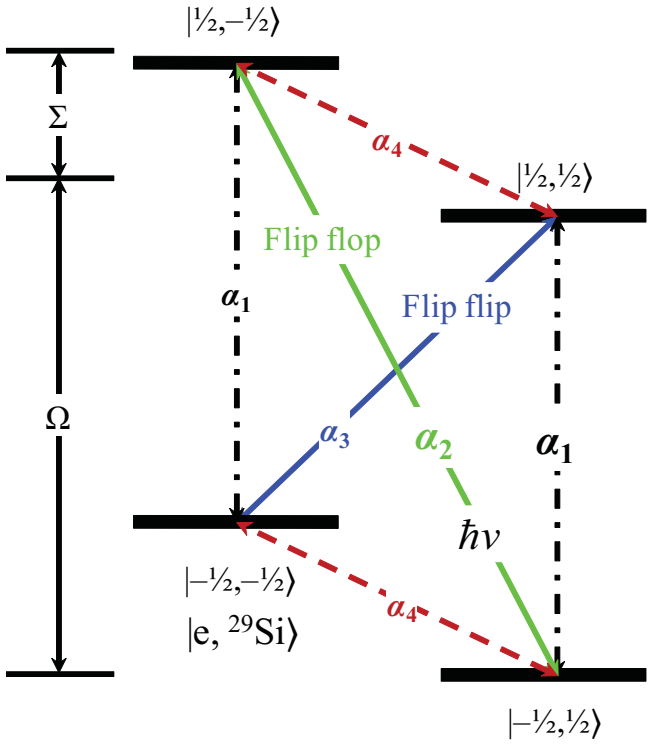

	I Thermal equilibrium	II Sat. α_3	III Sat. α_2	IV Sat. α_1
	$e^{-(\Omega+\Sigma)}$	$e^{-\Omega}$	1	1
	$e^{-\Omega}$	1	$e^{-\Omega}$	1
	$e^{-\Sigma}$	1	e^{Ω}	1
	1	e^{Ω}	1	1
Polarization →	$tanh(\Sigma/2)$	$tanh(\Omega/2)$	$tanh(\Omega/2)$	0

Figure 5.2: Magnetic energy level diagram and relaxation rate for the nuclear spin ($\boldsymbol{I}$ = ½) and the electron spins ($\boldsymbol{S}$ = ½) that are dipolar coupled in a dilute magnetic system. The relative populations are shown; in column (I) for thermal equilibrium, in columns II and III for dynamic nuclear polarization by saturation of forbidden transition (flip–flop (ΔM = 1, Δm = –1) or flip–flip (ΔM = 1, Δm = 1)), and (IV) for saturation of allowed transition leading to zero polarization.

We fix the magnetic field at the flip–flop transition which is one of the forbidden transitions in EPR. A strong microwave irradiation is used to induce the transitions between energy levels |½,–½⟩ and |–½,½⟩ (flip–flop transition) and flip–flip transitions between |½,½⟩ and |–½,–½⟩. The population will be determined by the electron spin relaxation rate because $\alpha_1 >> \alpha_2 = \alpha_3$. Therefore the population of |½,½⟩ and |–½,–½⟩ states will be maintained at $e^{-\Omega}$ and e^{Ω}, respectively. These dynamic populations yield a nuclear polarization

$$P = tanh(\Omega/2) = tanh\ (h\nu_e/2kT) \approx h\nu_e/2kT \tag{5.7}$$

which is larger than P_0 by the ratio $\nu_e/\nu_n = \gamma_e/\gamma_n$. Instead, if we saturate the *flip–flip* transition, the population of column (II) in Fig. 5.2 yields $P = tanh(\Omega/2)$. The polarization is equal but in reversed in sign compared to column (III). Saturation of the allowed transition at magnetic field $\boldsymbol{B}_0$ equalizes all the populations since $\alpha_2 = \alpha_3$. The nuclear polarization is zero, in this case.

5.1.3 Leakage factor

Assume that the microwave irradiation is set at the flip–flop transition and the strength of the source is such that the flip–flop transition rate (α_2) is much greater than the nuclear relaxation rate (α_4).

For a magnetically dilute system a small number of electron spins must interact with a large number n/N of nuclear spins. Consider first, a nuclear spin $\boldsymbol{I}$ that is ½. The entire electron spins $\boldsymbol{S}$ being ½, the spin $\boldsymbol{I}$ could only do a flip–flip transition, which is forbidden as it is off–resonance. On the other hand, a spin $\boldsymbol{I}$ that is –½ may do a flip–flop with a spin $\boldsymbol{S}$ that is ½, ending in a situation where $\boldsymbol{I}$ is ½ and $\boldsymbol{S}$ is –½. This spin $\boldsymbol{S}$, which is now –½, is dangers for all the $\boldsymbol{I}$ spins that are ½, since it could bring one of them to –½ through a forced flip–flop. In other words, it is essential for effective solid effect that each electron spin mutually flip a total number of n/N of nuclear spin via saturation of forbidden transition in time less than T_{1n}. To do this electron must have a relaxation time $T_{1e} < NT_{1n}/n$. Taking into account the above effect the leakage factor can be described as

$$f = \left(\frac{n}{T_{1n}}\right)\left(\frac{N}{T_{1e}}\right)^{-1} \tag{5.8}$$

where f is known as the leakage factor and T_{1n} and T_{1e} are the nuclear and electron spin lattice relaxation times, respectively. If the leakage factor is close to 1, the leakage factor will be a bottleneck in the in the enhancement (E) process by the following relation [116]

$$E = E_{max}\left(\frac{1}{1+f}\right), \tag{5.9}$$

where E_{max} is the maximum enhancement.

5.2 Dynamic nuclear polarization of ^{29}Si nuclei due to lithium related center

5.2.1 Experimental procedure

Naturally abundant silicon single crystal was grown along <100> direction and was cut in such a way that the face of the sample surface was (100), and the long axis was along [1$\bar{1}$0] crystal axis. Magnetic field rotates in (110) plane in such a way that it allows us to set the magnetic field parallel to the [100], [111] and [110] direction simply by rotation 0, 55, and 90 degrees, respectively as shown in Fig. 5.3. ^{nat}Si:Li^0 and ^{nat}Si:Li–O sample were prepared in the same way as mention in section 4.3.1. Before recording EPR spectra, both samples ^{nat}Si:Li^0 and ^{nat}Si:Li–O were etched in (HF + HNO_3) for 2 min to remove the surface defects. The EPR detection and DNP parameters for the isolated lithium and Li–O complex are listed in Table 5.1.

To perform DNP experiments, the EPR signal is saturated at high microwave power by fixing the magnetic field ($\boldsymbol{B}_{sat}$) at one point in the resonance line and at fixed temperature. Saturation was from 10 to 600 min to polarize ^{29}Si nuclear spins via solid effect. The transfer of the polarized sample from EPR to pulse nuclear magnetic resonance (NMR) spectrometers is performed with a disc permanent magnet placed on top of the sample to avoid the fast nuclear spin lattice relaxation in zero magnetic field.

Spinsight software that comes with the NMR spectrometer runs a pulse program that is written in *p*–code language. This program is used to apply pulse sequence and provide control of the electronic gates. If we turn on B_1 for a short time, the effective magnetic moment of ^{29}Si nuclei after DNP would precess through an angle $\theta = \gamma B_1 \Delta t$, where γ and Δt are the gyromagnetic ratio and pulse duration, respectively. After the $\pi/2$ pulse, the net magnetization will precesses in the

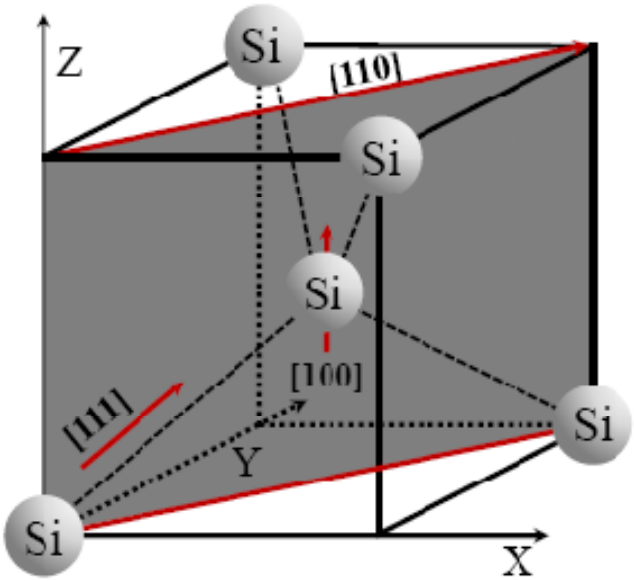

Figure 5.3: Schematic representation of major axes of our measurement. The external magnetic field ($\boldsymbol{B}_0$) rotates in (110) plane in such a way that magnetic field is parallel to [001], [111] and [110] directions and the angle on goniometer shows 0 degree, 55 degree and 90 degree, respectively.

X–Y plane, if there is any inhomogeneity in the static magnetic field B_0, the large ensemble of spins along X–Y plane in a sample will decay. The rate of this decay is termed T_2^*, and depends primarily on the field inhomogeneity and intrinsic decoherence time, T_2. We record this decay with time. This signal is called as a free induction decay signal (FID signal). The Fourier transformation will give ^{29}Si NMR signal. At π/2 pulse the ^{29}Si NMR intensity will be maximal. In order to decide the pulse length, we use powder of the naturally abundant silicon sample. After getting the π/2 pulse length, next step is to get the ^{29}Si NMR intensity at 300 K and 7 T. This value is known as the *thermal equilibrium* value. Each time we measure the ^{29}Si NMR signal after the DNP process, we calculate the degree of polarization and enhancement by using following expression;

$$Enhancement\ (E) = \frac{NMR\ Intensity_{DNP}}{NMR\ intensity_{Thermal\ equilibrium}} \frac{T}{300\ K} \frac{7\ \mathrm{T}}{B_0} \tag{5.10}$$

$$\text{DNP degree}(P_n^{ss}) = E \times Thermal\ equilibrium\ polarization\ at\ T\ and\ B_0 \qquad (5.11)$$

where T and $\boldsymbol{B}_0$ are the temperature and magnetic field at which DNP was performed, respectively.

Table 5.1: Typical values for the detection of EPR signal and DNP condition is listed for Li^0 and Li–O center in naturally abundance silicon.

Experimental parameters	**Electron paramagnetic Resonance**	**Dynamic nuclear polarization**
Center Field (B_0 / B_{sat})	322 mT	≈ 323 mT
Sweep Width	± 4 mT	---
Temperature (T)	3.4 – 20 K	3.4 – 20 K
Modulation Field	0.1 mT	0.1 mT
Power	1 mW	10 – 200 mW
Frequency	9.05 GHz	9.05 GHz
Saturation Time	----	0.1 – 10 hr

5.2.2 Saturation time dependence of ^{29}Si NMR signal

The ^{29}Si NMR signals detected after DNP were 10^2 – 10^3 times stronger than the signal detected from the control sample, i.e., the same sample without DNP but after keeping it in the magnetic field of 7 T at room temperature for 10–20 h. In this case the equilibrium Boltzmann nuclear polarization is $P_{n0} \cong 4.8\times10^{-4}$ %. The increase of NMR signals with the DNP time (t), i.e., duration of saturation in the EPR spectrometer, is shown in Fig. 5.4. These dependences are exponential and allow us to determine the nuclear polarization time T_{1n} and DNP degree P^{ss}_n by the extrapolation of the curves to the infinite saturation time. Such values for the lowest temperature obtained in this study T = 3.4 K are summarized in the Table 5.2. The DNP enhancement E^{ss} was determined with respect to the equilibrium nuclear spin polarization in the same magnetic field (≈323 mT). The Li–O centers EPR intensity is twice as high under band gap illumination compared to in dark for the temperature range 3.4 – 10 K. The possible reasons for

the change in EPR intensity are the increase in the absorption rate due to reduction in T_{1e} because the spin exchange between the photoexcited conduction electrons and donor electrons and enhancement in the Li–O donor concentration under illumination. Due to reduction in T_{1e}, fast mutual flipping of electron and ^{29}Si nuclear spin under saturation of forbidden transitions increases the effective DNP degree. The DNP degree also depends on the leakage factor which is proportional to T_{1e} [116]. Therefore the maximum DNP degree obtained in this study P^{ss}_n = 0.72 % was achieved at 3.4 K using Li–O EPR saturation of forbidden transition performed with halogen lamp illumination. The enhanced DNP degree under illumination was the combine effect of the reduced T_{1e} and donor concentration increment.

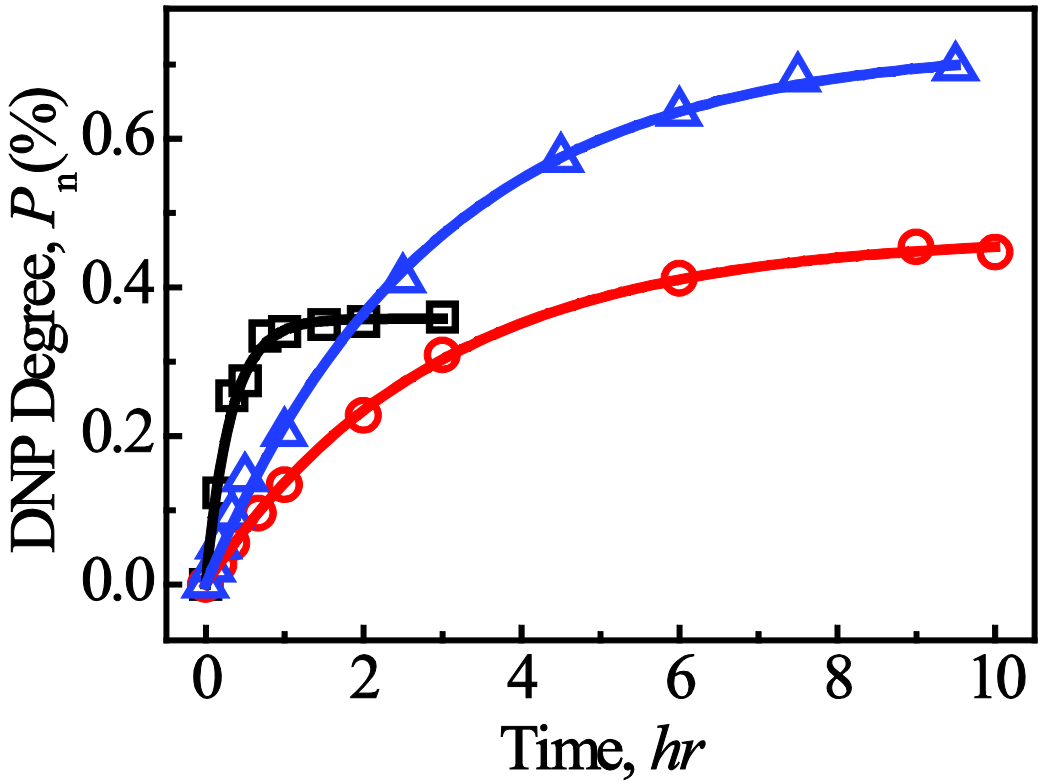

Figure 5.4: The DNP degree, P_n, vs. EPR saturation time, t, obtained without illumination at T=3.4 K in the samples containing Li^0 (□) and Li-O (○) centers and in the sample with Li-O center under illumination (△).

A ten times shorter nuclear polarization time T_{1n} observed in the samples containing Li^0 centers in comparison with the DNP caused by Li–O (Table 5.2) can also be attributed to shorter electron spin–lattice relaxation time T_{1e} of Li^0. The nuclear relaxation rate$1/T_{1n}$ is proportional to the concentration of paramagnetic centers N and to $1/T_{1e}$ [29, 109, 114]. Because concentrations of paramagnetic centers in our samples are approximately the same, the nuclear polarization time is determined by the electron spin–relaxation time which is shorter for Li^0 centers.

Table 5.2: The experimental result of ^{29}Si nuclei DNP is summarized. Temperature (T_s) and direction of polarization is listed and the polarization time T_{1n}, DNP degree P^{ss} obtained by extrapolation fitting to infinite saturation time, and DNP enhancement E^{ss} for Li^0, Li–O center in dark and light is mention.

Sample	T_s (K)	Orientation	T_{1n} (h)	$P^{ss}{}_n$ (%)	E^{ss}
^{nat}Si:Li^0		<100>	0.35	0.17	85
	3.4	<111>	0.33	0.35	170
		<110>	0.4	0.28	97
^{nat}Si:Li–O (dark)	3.4	<100>	3.0	0.46	225
		<110>	3.5	0.29	145
^{nat}Si:Li–O (light)	3.4	<100>	3.0	0.72	352
		<110>	2.7	0.48	235

5.2.3 Temperature and power dependence of ^{29}Si NMR signal

To get better ^{29}Si nuclei polarization degree we need to perform dynamic nuclei polarization technique at lower temperature. Figure 5.5 shows the temperature and power dependence of the ^{29}Si DNP degree for ^{nat}Si:Li^0 and ^{nat}Si:Li–O samples. We have discussed the EPR signal intensity temperature dependence of Li^0 and Li–O center in chapter 4. The lithium related center shows short relaxation time [47, 102] and possible to detect the DNP below 7 K. The temperature

dependence of the DNP degree for isolate lithium (Li^0), lithium–oxygen (Li–O) center under dark and illumination correlates well with the temperature dependences of the intensity of EPR spectra [see Fig. 4.6 (a)].

^{29}Si DNP degree varies roughly linearly with the microwave power in case of Li^0 that shows due to shorter electron spin lattice relaxation time, therefore it needs more power to saturate the electron spin resonance line to get better ^{29}Si nuclei polarization. Where as in case of Li–O center under illumination has shorter relaxation due to spin exchange with conduction electron and require more power to saturate EPR transition. Therefore Li^0 and Li–O center under light needs more microwave power to saturate the EPR forbidden transition.

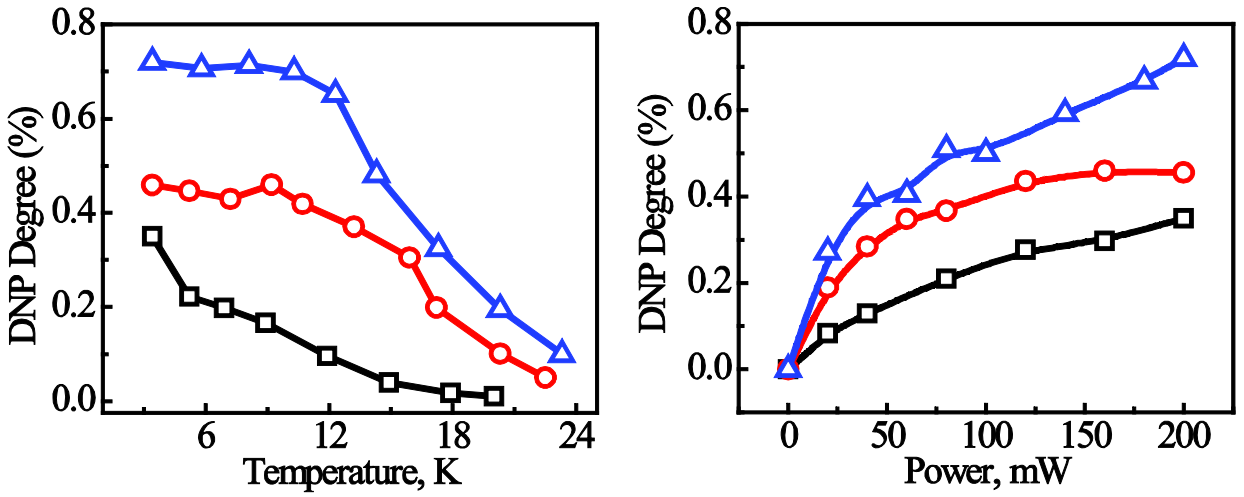

(a) (b)

Figure 5.5: The dependences of the ^{29}Si NMR intensity on the (a) temperature and (b) power of samples containing Li^0 (□) and Li–O (○) centers under dark and with illumination for Li–O center (△).

The efficiency of DNP can be defined as the degree of the equilibrium electron spin polarization that is transferred to nuclear spins by the DNP process, i.e., $k = P_n^{ss}/P_{e0}$. Figure 5.6 shows the dependence of k on the equilibrium electron polarization, which depends linearly on 1/T for all the experimental conditions ($\boldsymbol{B}_0$ = 320 mT, T = 3.4 – 20 K). The ^{29}Si DNP degree of Li–O complex under dark and light in the temperature range 3.4 – 10 K (Fig. 5.5 (a)) is higher than those of isolated Li as listed the DNP degree in Table 5.2. This reflects the highest DNP

efficiency of Li–O at 10 K because P_{e0} decreases exponentially with increasing temperature. The decrease in the DNP efficiency of Li–O at $T < 10$ K is due to the increase of the electron spin lattice relaxation time. The decrease in the efficiency of Li–O at $T > 10$ K is caused by ionization of the shallow donor levels. To evaluate the DNP efficiency quantitatively need to know the exact value of T_1 and number of donor under illumination whereas we evaluate the DNP efficiency qualitatively that confirm that at low temperature higher degree of electron polarization produce higher degree of polarization.

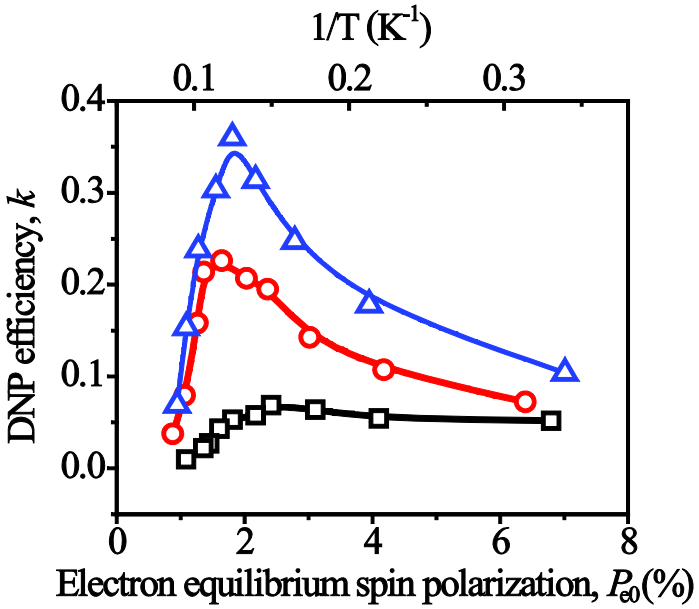

Figure 5.6: The DNP efficiency *k,* vs. equilibrium electron spin polarization degree (P_{e0}), for samples containing Li^0 (□), Li–O (○) under dark and illumination (△).

5.2.4 Field dependence of ^{29}Si NMR signal

DNP of ^{29}Si nuclear spins was observed in all of the investigated samples under saturation of EPR lines of both the Li^0 and Li–O centers. Figure 5.7 shows the enhanced ^{29}Si NMR signal intensities (red open circles) after saturation of the Li^0 EPR transition in the magnetic field given

by the horizontal axis. Figure 5.7 also shows the EPR lines intensity (black solid curve) for comparison.

Figure 5.8 shows the same plot for the Li–O centers in different orientation and under light and dark. If *Overhauser effect* is a dominate mechanism in our sample the peak of ^{29}Si NMR signal should appear at $\boldsymbol{B}_{sat} - \boldsymbol{B}_0 = 0$. The fact is that it is not the case in both Fig. 5.7 and 5.8 gives clear evidence that the DNP of ^{29}Si nuclei is the result of the *solid effect* which is due to the saturation of electron spin resonance forbidden transition. The experimental error in the peak position of ^{29}Si NMR intensity is 0.01 mT which is sufficient to distinguish the mechanism of DNP of ^{29}Si nuclei. For the possibility of contribution of *Overhauser effect* is overruled because *Overhauser effect* only possible for concentrations range of 5×10^{17} cm^{-3}. The shift, $\Delta B_{\pm}$, of the forbidden "flip–flop" and "flip–flip" transitions from the center of ESR line for $B_0 \cong 323$ mT is approximately $\Delta B_{\pm} = \boldsymbol{B}_{sat} - \boldsymbol{B}_0 = \pm \boldsymbol{B}_0(\gamma_n/\gamma_e) \approx \pm 0.1$ mT for the ^{29}Si nuclei. Indeed, for the case of the DNP with Li^0 centers, the spacing between maximal positive and negative.

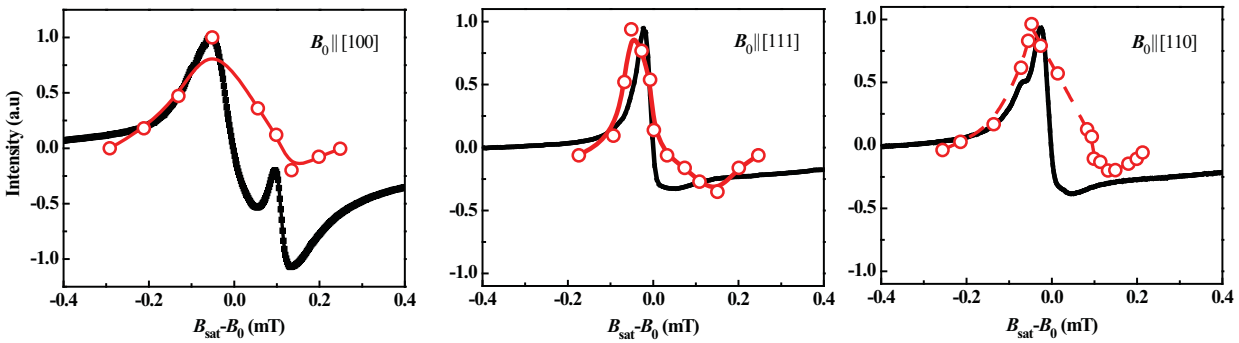

Figure 5.7: The increased (> 0) or decreased (< 0) ^{29}Si NMR signal intensities (O) after saturation of the Li^0 EPR transition in the magnetic field given by the horizontal axis and the direction indicated in the Figure. The horizontal axis shows the deviation of the magnetic field $\boldsymbol{B}_{sat}$ from the field $\boldsymbol{B}_0$ that gives the maximum of Li^0 EPR line. The solid curves show the first derivative of the Li^0 EPR absorption lines. The ^{29}Si NMR signals were acquired at $T = 300$ K and $\boldsymbol{B}_0 = 7$ T after microwave saturation with microwave power of 200 mW during 10 minutes at $T_s = 3.4$ K. The positive and negative signs of the NMR signals correspond to DNP in the opposite and the same directions with respect to equilibrium nuclear polarization.

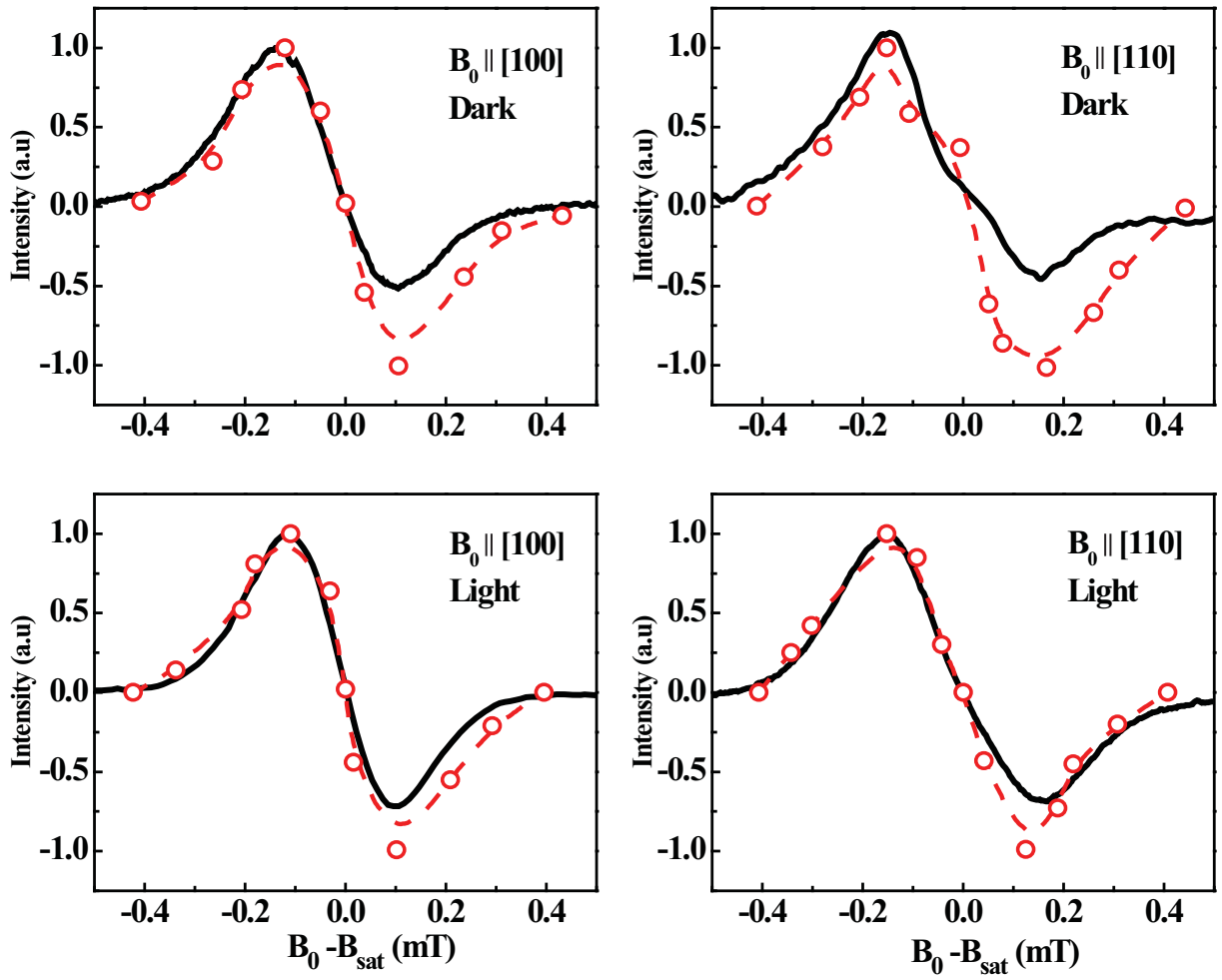

Figure 5.8: The dependences of the ^{29}Si NMR signal intensity is represented by (O) after 10 min of EPR line saturation on the deviation of the magnetic field $\boldsymbol{B}_{sat}$ from the center of the Li–O EPR line $\boldsymbol{B}_0$ and the first derivative of the EPR line (solid lines) without illumination and under illumination at the orientation of magnetic field along <100> and <110> crystal axis.

DNP–NMR signals slightly exceed the Li^0 EPR linewidth that is narrower than 0.2 mT. This is a typical case of the so–called partly resolved solid–effect [116], where forbidden flip–flop and flip–flip transitions occur at the magnetic field just outside of the EPR linewidth. This explains why the dependence of the DNP–NMR signals does not follow exactly the EPR first derivative line–shape of the Li^0 center (Fig. 5.7). On the other hand the EPR linewidth of the Li–O center is much larger than that of Li^0 and the NMR intensity shape agrees very well with the EPR first

derivative line–shape (Fig. 5.8). In this case the flip–flop and flip–flip transitions are buried within the linewidth of the inhomogeneously broadened EPR peak.

5.3 Towards further improvement of DNP using Li related centers

We have observed that EPR spectrum of the Li related center was not fully saturated at 200 mW microwave power due to its short T_{1e} and the EPR line showing inhomogeneous broadening characteristics. So, it would be desirable to use higher microwave power to saturate transitions, which would help to achieve higher nuclear spin polarizations and lower nuclear polarization time (T_{1n}). Moreover, the differential solid effect due to inhomogeneous broadening reduces the polarization in our system [116], which can be overcome by using *integrated solid effect* (ISE) [117] or by the *nuclear spin orientation via electron spin locking* (NOVEL) method [118]. NOVEL can be more effective than ISE for Li related centers due to its short T_{1e}. On the other hand, Li – O center is more efficient for the case of integrated solid effect.

The broadening of the Li^0 EPR lines is caused by random internal stress. Applying external uniaxial stress the Li^0 EPR line width can be reduced significantly and a higher DNP can be achieved [46].

^{28}Si isotopically enrich samples can also be used to eliminate the inhomogeneous broadening of the EPR lines of Li related centers. We can also achieve higher polarization of ^{29}Si using samples with donor concentration ~10^{17} cm^{-3}, as shown by Dementyev *et al.* where they have reported 10.0±3.4 % ^{29}Si polarization by donor electrons via the *Overhauser* mechanism within exchange–coupled donor clusters in phosphorus and antimony doped single crystal silicon [119]. Lithium can be a good candidate for the above mechanism as its short electron spin lattice relaxation time allows for working at much lower temperatures. Higher magnetic fields at lower temperatures lead to higher electron polarization that can interact with ^{29}Si nuclei.

5.4 Summary

The EPR spectrum of the Li related donor center in FZ Si that was observed in the 3.4–20 K range under absorption mode allows us to perform the DNP experiment at low temperature. The temperature and power dependence of ^{29}Si NMR intensity confirm that the T_{1e} of Li and Li–O complex under light has shorter relaxation than the Li–O complex under dark. The field dependence of ^{29}Si nuclei polarization was investigated in detail to show that the DNP was dominated by the solid effect for both neutral Li and Li–O complex centers. Higher DNP of ^{29}Si nuclei produced by Li related centers than those by phosphorus was observed at low temperature (3.4 K). Saturation of the Li–O complex EPR transition under illumination gives a 352 fold enhancement and 0.72 % polarization of ^{29}Si nuclei.

Chapter 6

Conclusion

The present thesis reported investigations of magnetic properties of lithium (Li) hydrogenic donor related centers in silicon by electron paramagnetic resonance (EPR) spectroscopy and interaction of Li–related centers with host ^{29}Si nuclear spins by nuclear magnetic resonance (NMR) spectroscopy. Lithium is the only non–substitutional hydrogenic donor in silicon that forms a complex pair with an oxygen atom very easily.

Significant narrowing of the isolated Li EPR and additional hyperfine structures of lithium–oxygen (Li–O) centers were observed in isotopically enriched ^{28}Si single crystals. Unexpected splitting was found reflecting the principal axis of the formally assigned trigonal *g*–tensor being 3^{o} tilted from <111> crystal axis, i.e., the g–tensor of the Li–-O center actually has a monoclinic symmetry. Furthermore splitting of ^{7}Li hyperfine lines into four components was observed at temperatures 3.5 K. These findings provided accurate knowledge of EPR frequencies of Li related centers that are needed for high fidelity operation of Li quantum bits in silicon.

Dynamic nuclear polarization (DNP) of ^{29}Si nuclear spins were induced by saturation of EPR transitions of lithium–related centers. Both isolated Li and Li–O complex centers showed strong EPR absorption lines in the temperature range 3.4–10 K and led to very efficient orientation of ^{29}Si nuclear spins. The temperature dependence and time constant of ^{29}Si DNP are investigated in detail. The ^{29}Si DNP of 0.72 % was achieved at 3.4 K by excitation of the Li-O forbidden EPR transition under illumination, corresponding to a ~352 fold increase with respect

to the thermal equilibrium polarization. Possible strategies are discussed to obtain >5% ^{29}Si DNP that is needed for realization of quantum computing.

Reference

[1] P. W. Shor, *Algorithms for quantum computation: Discrete logarithms and factoring*, Proc. 35th Annual Symposium on the Foundations of Computer Science, IEEE Computer Society, 1994, p. 124.

[2] P. W. Shor, *Polynomia–time algorithms for prime factorization and discrete logarithms on a quantum computer*, SIAM J. Compt. 26 (1997), 1484.

[3] L. K. Grover, *A fast quantum mechanical algorithm for database search*, Proc. 28th Annual ACM Symposium on the Theory of computing, 1996, p. 212.

[4] R. P. Feynman, *Simulating physics with computers*, Int. J. Theor. Phys., **21** (1982), 467.

[5] D. Deutsch, *Quantum theory, the Church–Turing principle and the universal quantum computer*, Proc. R. Soc. Lond. A, **400** (1985), 97.

[6] *D. P. DiVincenzo, Quantum Computation, Science 270 (1995), 255.*

[7] B. E. Kane, *A silicon–based nuclear spin quantum computer*, Nature (London) **393** (1998), 133.

[8] G. Burkard, H. A. Engel, and D. Loss, *Spintronics and quantum dots for quantum computing and quantum communication*, Fortschritte Der Physik, 48 (2000), 965.

[9] S. A**.** Lyon, *Spin–based quantum computing using electrons on liquid helium*, Phys. Rev. A **74** (2006), 052338.

[10] W. Harneit, *Fullerene–based electron–spin quantum computer*, Phys. Rev. A **65** (2002), 032322.

[11] A. Ardavan, M. Austwick, S. C. Benjamin, G. A. D. Briggs, T. J. S. Dennis, A. Ferguson, D. G. Hasko, M. Kanai, A. N. Khlobystov, B. W. Lovett, G. W. Morley, R. A. Oliver, D. G. Pettifor, K. Porfyrakis, J. H. Reina, J. H. Rice, J. D. Smith, R. A. Taylor, D. A. Williams, C. Adelmann, H. Mariette, and R. J. Hamers, *Nanoscale solid–state quantum computing*, Phil. Trans. R. Soc. A **361** (2003), 1473.

[12] J. I. Cirac and P. Zoller *Quantum computations with cold trapped ions*, Phys. Rev. Lett. **74** (1995), 4091.

[13] I. L. Chuang and Y. Yamamoto, *Simple quantum computer*, Phys. Rev. A **52** (1995), 3489.

[14] M. Mehring, J. Mende, and W. Scherer, *Entanglement between an electron and a nuclear spin ½*, Phys. Rev. Lett. **90** (2003), 153001.

[15] Q. A. Turchette, C. J. Hood, W. Lange, H. Mabuchi, and H. J. Kimble, *Measurement of conditional phase shifts for quantum logic*, Phys. Rev. Lett. **75** (1995), 4710.

[16] Z–B. Chen, and Y–D. Zhang, *Possible realization of Josephson charge qubits in two coupled Bose–Einstein condensates*, Phys. Rev. A **65** (2002), 022318.

[17] D. Loss and D. P. DiVincenzo, *Quantum computation with quantum dots*, Phys. Rev. A **57** (1998), 120.

[18] J. E.Mooij, T. P. Orlando, L. Levitov, L. Tian, C. H. van der Wal, and S. Lloyd, *Josephson persistent–current qubit*, Science **285** (1999), 1036.

[19] E. Biolatti, I. d'Amico, P. Zanardi, and F. Rossi, *Electro–optical properties of semiconductor quantum dots: Application to quantum information processing*, Phys. Rev. B **65** (2002), 075306.

[20] S. Lloyd, *A potentially realizable quantum computer*, Science **261** (1993), 1569.

[21] D. G. Cory, A. F. Fahmy, and T. F. Havel, *Ensemble quantum computing by NMR spectroscopy*, Proc. Natl. Acad. Sci. **94** (1997), 1634.

[22] T. D. Ladd, J. R. Goldman, F. Yamaguchi, Y. Yamamoto, E. Abe, and K. M. Itoh, *All–Silicon quantum computer*, Phys. Rev. Lett. **89** (2002), 017901.

[23] K. M. Itoh, *An all–silicon linear chain NMR quantum computer*, Solid State Commun. **133** (2005), 747.

[24] V. N. Smelyanskiy, A. G. Petukhov, V. V. Osipov, *Quantum computing on long–lived donor states of Li in Si*, Phys. Rev. B **72** (2005), 081304(R).

[25] L. Chernyak, V. Lyakhovitskaya, and D. Cahen, *Low temperature device creation in Si via fast Li electromigration*, Appl. Phys. Lett. **66** (1995), 709.

[26] T. E. Gilmer Jr., R. K. Franks, R. J. Bell**,** *An optical study of lithium and lithium oxygen complexes as donor impurities in silicon*, J. Phys. Chem. Solid 26 (1965), 1195.

[27] R. L. Aggarwal, P. Fisher, V. Mourzine, and A. K. Ramdas, *Excitation spectra of lithium donors in silicon and germanium*, Phys. Rev. **138** (1965), A882.

[28] G. Feher, and E. A. Gere, *Electron spin resonance experiments on donors in silicon. II. Electron spin relaxation effects*, Phys. Rev. **114** (1959) 1245.

[29] H. Hayashi, W. Ko, T. Itahashi, A. Sagara, K. M. Itoh, L. S. Vlasenko, and M. P. Vlasenko, *Dynamic nuclear polarization of ^{29}Si nuclei in the isotope enriched n-type silicon*, phys. Status Solidi C **3** (2006), 4388.

[30] H. Hayashi, T. Itahashi, K. M. Itoh, L. S. Vlasenko, and M. P. Vlasenko, *Dynamic nuclear polarization of ^{29}Si nuclei in isotopically controlled phosphorus doped silicon,* Phys. Rev. B **80** (2009), 045201.

[31] W. Kohn, *Solid State Physics*, edited by F. Seitz and D. Turnbull (Acad. Press Inc., New York) **5** (1957), 257.

[32] C. S. Fuller and J. A. Ditzenberger, *Diffusion of lithium into germanium and silicon*, Phys. Rev. **91** (1953), 193.

[33] B. Goldstein, *Direct observation of lithium–defect interaction in silicon by electron paramagnetic resonance measurements*, Phys. Rev. Lett. **17** (1966), 428.

[34] D. A. Jackson and H. Kuhn, *Hyperfine structure and Zeeman–effect of the resonance lines of lithium*, Proc. Roy. Soc. Lond. A **173** (1939), 278.

[35] M.Fox and I. I. Rabi, *On the nuclear moments of lithium, potassium, and sodium*, Phys. Rev. **48** (1935), 746.

[36] H. J. Guislain, W. K. Schoenmaekers, and L. H. De Laet, *On the behavior of lithium in silicon*, Nuclear Instrum. and Methods **101** (1972), 1.

[37] F. S. Goulding, *Semiconductor detectors for nuclear spectrometry*, I. Nucl. Instrum. Methods **43** (1966), 1.

[38] J. W. Mayer, *Semiconductor detectors for nuclear spectrometry*, II. Nucl. Instrum. Methods **43** (1966), 55.

[39] J. M. Hollander, *The impact of semiconductor detectors on gamma-Ray and electron spectroscopy*, Nucl. Instrum. Methods 43 (1966), 65.

[40] E. S. Johnson, W. D. Compton, J. R. Noonan and B. G. Streetman, *Recombination luminescence from electron–irradiated Li–diffused Si*, J. Appl. Phys. **44** (1973), 5411.

[41] H. Neubrand, *Nachweis von Sauerstoff in Silizium-Einkristallen mittels ESR*, Phys. Stat. Sol. (a) **17** (1973), 459.

[42] M. Laguës, J. L. Domange and J. P. Hurault, *Segregation of dissolved Li to the surface of Si: A new activation process*, Solid State commun. **12** (1973), 203.

[43] A. J. R. De Kock, *Vacancy clusters in dislocation–free silicon,* Appl. Phys. Lett. **16** (1970), 100.

[44] A. A. Kastalskii and S. B. Maltsev *"Condensation" of impurities in semiconductors (Si + Li)*, Solid State commun. **17** (1975), 107.

[45] J. H. Rose, H. B. shore, and E. Zaremba, *Condensed phase of lithium impurities in silicon*, Phys. Rev. Lett., **37** (1976), 354.

[46] G. D. Watkins and F. S. Ham, *Electron paramagnetic resonance studies of a system with orbital degeneracy: The lithium donor in silicon,* Phys. Rev. B **1** (1970), 4071.

[47] G. Feher, *Electron spin resonance experiments on donors in silicon. I. Electronic structure of donors by the electron nuclear double resonance technique*, Phys. Rev. **114** (1959), 1219.

[48] O. K. Rice, *Electronic Structure and Chemical Bonding* (McGraw. Hill Book Company, Inc., New York, 1940), Chap. XIV.

[49] C. S. Fuller, *Diffusivity and solubility of copper in germanium*, Phys. Rev. **86** (1952), 136.

[50] C. S. Fuller, H. C. Theuerer and W. W. Van Roos-Broeck, *Properties of thermally produced acceptors in germanium*, Phys. Rev. **85** (1952), 678.

[51] C. S. Fuller and J. C. Severiens, *Mobility of impurity ions in germanium and silicon*, Phys. Rev. **96** (1954), 21.

[52] E. M. Pell, *Interaction between Li and O in Si*, presented at the Brussels conference, 1958.

[53] F. S. Ham, *Theory of diffusion-limited precipitation*, J. Phys. Chem. Solids **6** (1958), 335.

[54] E. M. Pell, *Ion drift in an n–p junction*, J. Appl. Phys. **31** (1960), 291.

[55] W. Kaiser and P. H. Keck, *Oxygen content of silicon single crystals*, J. Appl. Phys. **28** (1957), 882.

[56] W. Kaiser, P. H. Keck, and C. F. Lange, *Infrared absorption and oxygen content in silicon and germanium*, Phys. Rev. **101** (1956), 1264.

[57] C. A. Wert and C. Zener, *Interstitial atomic diffusion coefficients*, Phys. Rev. **76** (1949), 1169.

[58] C. Zener, *Relation between residual strain energy and elastic moduli*, Acta. Cryst. **2** (1949), 163.

[59] R. A. Swalin, *Theoretical calculations of the enthalpies and entropies of diffusion and vacancy formation in semiconductors*, J. Phys. Chern. Solids **18** (1961), 290.

[60] K. Weiser, *Theory of diffusion and equilibrium position of interstitial impurities in the diamond lattice*, Phys. Rev. **126** (1962), 1427.

[61] M. Born and K. Huang, *Dynamical Theory of Crystal Lattices* (Oxford University Press, New York, 1954), Chap. I.

[62] M. Born and K. Huang, *Dynamical Theory of Crystal Lattices* (Oxford University Press, New York), 1954, Chap. 1.

[63] C. Kittel, *Introduction to Solid–State Physics*, J. Wiley & Sons, Inc., New York, (1956) Chap 1.

[64] C. J. F. Bottcher, *Theory of Electric Polarization*, (Elsevier Publishing Company, Inc., New York, 1952), Chap. V.

[65] L. Bellomonte and M. H. L. Pryce, *Vibrations of interstitial Li^+ ions in silicon I. Force constants*, Proc. Phys. Soc. Lond. **89** (1966), 967.

[66] L. Bellomonte and M. H. L. Pryce, *Vibrations of interstitial Li^+ ions in silicon II. Frequency of localized vibration mode*, Proc. Phys. Soc. Lond. **89** (1966), 973.

[67] P. J. Price, *Theory of transport effects in semiconductors: Thermoelectricity*, Phys. Rev. **104** (1956), 1223.

[68] D. K. Wilson and G. Feher, *Electron spin resonance experiments on donors in silicon. III. Investigation of excited states by the application of uniaxial stress and their importance in relaxation processes*, Phys. Rev. **124** (1961), 1068.

[69] R. L. Aggarwal and A. K. Ramdas, *Effect of uniaxial stress on the excitation spectra of donors in silicon*, Phys. Rev. **137** (1965), A602.

[70] R. L. Aggarwal, *Optical detection of the valley–orbit splitting of the ground state of donors in silicon*, Solid State commu. **2** (1964), 163.

[71] J. H. Reuszer and P. Fisher, *An optical determination of the ground–state splittings of Group–V impurities in germanium*, Phys. Rev. **135** (1964), A1125.

[72] C. Jagannath, Z. W. Grabowski and A. K. Ramdas, *Linewidth of electronic excitation spectra of donor in silicon*, Phys. Rev. B **23** (1981), 2082.

[73] C. Herring and E. Vogt, *Transport and deformation–potential theory for many–valley semiconductors with anisotropic scattering*, Phys. Rev. **101** (1956), 944.

[74] A. Honig and A. F. Kip, *Electron spin resonance of impurity level in silicon*, Phys. Rev. **95** (1954), 1686.

[75] A. F. Kip, C. Kittel, R. A. Levy, and A. M. Portis, *Electronic structure of F–centers: Hyperfine interactions in electron spin resonance*, Phys. Rev. **91** (1953), 1066.

[76] A. M. Portis, *Electronic structure of F–centers: Saturation of the electron spin resonance*, Phys. Rev. 91 (1953), 1071.

[77] G. Feher, J. C. Hensel, and E. A. Gere, *Paramagnetic resonance absorption from acceptors in silicon*, Phys. Rev. Lett. **5** (1960), 309.

[78] M. Höhne, *EPR of lithium in mechanically affected silicon*, Phys. Status Solidi B **85** (1978), 525.

[79] P. Fisher and R. E. M. Vickers, *Bulk stress due to surface damage of crystalline silicon and germanium*, Appl. Phys. Lett. **79** (2001), 3458.

[80] G. Feher, *Observation of nuclear magnetic resssonances via the electron spin resonance line*, Phys. Rev. **103** (1965), 834.

[81] W. Gerlach and O. Stern, *Der experimentelle Nachweis des magnetischen moments des silberatoms*, Z. Phys. **8** (1922), 110.

[82] W. Gerlach and O. Stern, *Der experimentelle Nachweis des richtungsqantelung im magnetfeld*, Z. Phys. **9** (1922), 349.

[83] G. E. Uhlenbeck and S. Goudsmit, *Spinning electrons and the structure of spectra*, Nature **117** (1926), 264.

[84] G. Breit and I. I. Rabi, *Measurement of nuclear spin*, Phys. Rev. **38** (1931), 2082.

[85] I. I. Rabi, S. Millman, J. R. Zacharias, and P. Kusch, *A new method of measuring nuclear magnetic moment*, Phys. Rev. **53** (1938), 318.

[86] E. Zavoisky, J. Phys. USSR **9** (1945), 245.

[87] E. Zavoisky, *Paramagnetic resonance absorption in orthogonal and parallel fields for salt, solution and metals*, PhD thesis in Russia (1944) at Kazan University.

[88] J. Frenkel, *On the theory of relaxation losses, connected with magnetic resonance in solid bodies*, J. Phys. USSR **9** (1945), 299.

[89] R. L. Cummerow and D. Halliday, *Paramagnetic losses in two manganous salts*, Phys. Rev. **70** (1946), 433.

[90] D. M. S. Bagguley and J. H. E. Griffiths, *Paramagnetic resonance and magnetic energy levels in chrome alum*, Nature **160** (1947), 532.

[91] A. A. Galkin, O. Y. Grinberg, A. A. Dubinskii, N. N. Kabdin, V. N. Krymov, V. I. Kurochkin, Y. S. Lebedev, L. G.Oranskii and V. F. Shuvalov, *EPR spectroscopy in 2–mm range for chemical–research*, Instr. and Exp. Tech. **20** (1977), 1229.

[92] J. H. Van Vleck, *The theory of electric and magnetic susceptibility*, Oxford University Press, London, U. K., 1932, p. 3.

[93] A. Abragam, *Time reversal*, Charendon Press, Oxford, U. K., (1989).

[94] F. Bloch, *Nuclear induction*, Phys. Rev. **69** (1946), 127.

[95] C. P. Slichter, Principle of magnetic resonance, 3rd ed., Springer, New York, (1990), Chap. 2.

[96] R. G. Shulman and B. J. Wyluda, *Nuclear magnetic resonance of ^{29}Si in n– and p–type silicon*, Phys. Rev. **103** (1956), 1127.

[97] R. C. Fletcher, W. A. Yager, G. L. Pearson, and F. R. Merritt, *Hyperfine splitting in spin resonance of Group V donors in silicon,* Phys. Rev. **95** (1954), 844.

[98] R. C. Fletcher, W. A. Yager, G. L. Pearson, and F. R. Merritt, *Spin resonance of donors in silicon*, Phys. Rev. **94** (1954), 1392.

[99] W.Kohn and J. M. Luttinger, *Hyperfine splitting of donor states in silicon*, Phys. Rev. **97** (1955), 883.

[100] C. P. Slichter, Principle of magnetic resonance, 3rd ed., Springer, New York, (1990), Chap. 10.

[101] M. Höhne, *Nonrandom strain in ^{29}Silicon*, Phys. Status Solidi B **86** (1978), 119.

[102] V. N. Smelyanskiy, A. G. Petukhov, A. M. Tyryshkin, S. A. Lyon. T. Schenkel, J. W. Ager, and E. E. Haller, *Chiral symmetry and electron spin relaxation of lithium donor in silicon,* arXiv: 0807 (2008) 3928.

[103] A. Honig, Proceedings of the Kamerlingh–Onnes Memorial Conference on Low–Temperature Physics, Leiden, Holland, 1958 [Supp!. Physica 24, Sept. (1958)].

[104] G. Feher and R.C. Fletcher, Bull. Am., Phys. Soc. Ser. II **1** (1956), 125.

[105] E. Abe, A. M. Tyryshkin, S. Tojo, John J.L. Morton, W. M. Witzel, A. Fujimoto, J. W. Ager, E. E. Haller, J. Isoya, S. A. Lyon, M. L. Thewalt, and K. M. Itoh, *Electron spin coherence of phosphorus donors in silicon: Effect of environmental nuclei*, Phys. Rev. B **82** (2010), 121201.

[106] H. Tezuka, A. R. Stegner, A. M. Tyryshkin, S. Shankar, M. L. W. Thewalt, S. A. Lyon, K. M. Itoh, and M. S. Brandt, *Electron Paramagnetic Resonance of*

Boron Acceptors in Isotopically Purified Silicon, Phys. Rev. B **81** (2010), 161203(R).

[107] A. Abragam and B. Bleaney, *Electron paramagnetic resonance of transition ions* Clarendon Press, Oxford, 1970.

[108] C. A. J. Ammerlaan, *Paramagnetic centers in silicon*, Landolt.B¨ornstein Numerical Data and Functional Relationship in Science and Technology / Ed. by O. Madelung. Vol. 22 b, Impurity and Defects in Group IV Elements and III and V Compounds, Springer Verlag Berlin (1992), p 365.

[109] C. J. Gorter, *A new suggestion for aligning certain atomic nuclei*, Physica **14** (1948), 504;

[110] M. E. Rose, *On the Production of Nuclear Polarization*, Phys. Rev.**75** (1949), 213.

[111] A. W. Overhauser, *Polarization of nuclei in metals*, Phys. Rev. **92** (1953), 411.

[112] C. D. Jeffries, *Polarization of nuclei by resonance saturation in paramagnetic crystals*, Phys. Rev. **106** (1957), 164. [102]

[113] A. Abragam, *Overhauser effect in nonmetals*, Phys. Rev. **98** (1955), 1729.

[114] A. Abragam, *The Principles of nuclear magnetism* (Clarendon Press, Oxford 1961), p. 354.

[115] A. Abragam, J. Combrisson, and I. Solomon, *Polarisation dynamique des noyaux du silicium 29 dans le silicium a 4.2* K, C. R. Acad. Sci. **247** (1958) 2337.

[116] O. S. Leifson and C. D. Jeffries, *Dynamic polarization of nuclei by electron–nuclear dipolar coupling in crystals*, Phys. Rev. **122** (1961), 1781.

[117] A. Henstra, P. Dirksen, and W. Th. Wenckebach**,** *Enhanced dynamic nuclear polarization by the integrated solid effect*, Phys. Lett. A **134** (1988), 134.

[118] A. Henstra, P. Dirksen, J. Schmidt, and W.Th. Wenckebach, *Nuclear spin orientation via electron spin locking* (*NOVEL*), J. Magn. Reson. **77** (1988), 389.

[119] A. E. Dementyev, D. G. Cory, and C. Ramanathan, *Dynamic nuclear polarization in intermediately-doped single crystal silicon*, arXiv:0903.4699v2 (2009).